Monthly Notices of the ROYAL ASTRONOMICAL SOCIETY

MNRAS **543,** 1373–1392 (2025) https://doi.org/10.1093/mnras/staf1491
Advance Access publication 2025 September 08

SNELLS-HD – I. A first look at the stellar properties of the massive strong-lens galaxy SNL-1 with 50 pc resolution

Adriano Poci [1,2]★ and Russell J. Smith [2]

[1]*Astrophysics Sub-department, Department of Physics, University of Oxford, Keble Road, Oxford OX1 3RH, UK*
[2]*Centre for Extragalactic Astronomy, University of Durham, Stockton Road, Durham DH1 3LE, UK*

Accepted 2025 September 1. Received 2025 August 31; in original form 2024 August 2

ABSTRACT

We present a dynamical and chemical study of the centre of a massive early-type strong-lens galaxy ESO 286−G022 (SNL-1). Analysing new data obtained through the adaptive-optics-assisted Narrow-Field Mode of Very Large Telescope/Multi-Unit Spectroscopic Explorer, we aim to measure the mass distribution and internal properties of SNL-1 at ∼50 pc resolution. In particular, we aim to address the tension in the reported initial mass function (IMF) measurements of SNL-1 between strong-lens/dynamical and spectral-fitting techniques. We fit a triaxial orbital dynamical model to the measured stellar kinematics, including constraining the mass of the (resolved) central supermassive black hole. The dynamical model is consistent with the mass-to-light ratio expected for a Kroupa-like IMF. We also employ a highly flexible spectral-fitting technique, which instead favours a Salpeter-like IMF (low-mass slope $\alpha \approx 2.3$) over the same spatial region. To conclude, we discuss possible origins of this discrepancy, both intrinsic and technical.

Key words: galaxies: elliptical and lenticular, cD – galaxies: kinematics and dynamics – galaxies: stellar content – galaxies: structure.

1 INTRODUCTION

Massive early-type galaxies (ETGs) are the end product of galaxy evolution processes. As such, their physical properties encode information about said processes, and are therefore a useful tool for studying how galaxies form and evolve. In particular, the centre of ETGs gives us access to a physical regime not found elsewhere. It is for this reason that they have been the focus of study for many years.

In general, the centres of massive ETGs are characterized by extreme stellar densities, stellar metallicities, and old stellar populations, a dearth of gas, and dynamically hot orbital configurations (e.g. de Zeeuw & Franx 1991; Cappellari 2016). This is believed to be the result of an initial, intense burst of *in situ* star formation at early times, followed by more passive evolution through the accretion of lower mass galaxies (e.g. Naab, Johansson & Ostriker 2009; Oser et al. 2010; Zibetti et al. 2020).

Observations of the centres of massive ETGs provided indications that they formed with extreme stellar initial mass functions (IMFs), having an abundance of low-mass stars many times greater than what was found for the solar neighbourhood – a so-called 'bottom-heavy' IMF (e.g. Spiniello et al. 2011; Dutton, Mendel & Simard 2012; Smith et al. 2015b; Lyubenova et al. 2016; La Barbera et al. 2017; van Dokkum et al. 2017; Vaughan et al. 2018). Yet concurrently, evidence was emerging that disfavoured such dwarf-rich IMF (e.g. Brewer et al. 2012; Davis & McDermid 2017; Alton, Smith & Lucey 2018; Collier, Smith & Lucey 2018b), using different techniques and galaxy samples between all of these works. This tension has been explicitly investigated with the analysis of Smith (2014), which compared the different IMF measurement techniques on the same sample of galaxies, concluding that indeed the methodologies themselves produced incompatible results. A similar conclusion was drawn from the work of Smith et al. (2015b). In order, therefore, to make progress on the intrinsic IMF variations within galaxies, these technical differences must first be understood.

One particular galaxy for which different measurement techniques provide inconsistent results is ESO 286−G022 (hereafter SNL-1), discovered as part of the SINFONI Nearby Elliptical Lens Locator Survey (SNELLS; Smith, Lucey & Conroy 2015a). Strong gravitational lensing, in combination with dynamical models, provides a mass-based estimate of the stellar IMF by marginalizing over the dark matter (DM) contribution. For SNL-1, this approach yields a stellar mass-to-light ratio ($M_\star/L$) consistent with a Kroupa (2001) IMF (Newman et al. 2017). Refining the lens model, Collier, Smith & Lucey (2018a) found an 'IMF mismatch' $\alpha_{\rm IMF} = \Upsilon_{\rm lens}/\Upsilon_{\rm Kroupa} = 1.17 \pm 0.09$ for lensing and reference mass-to-light ratios $\Upsilon_{\rm lens}$ and $\Upsilon_{\rm Kroupa}$, respectively. The $M_\star/L$ from the lensing is thus consistent with that predicted from a Kroupa (2001) IMF (with a slightly higher abundance of dwarf stars). While there is a range of possible values of $\alpha_{\rm IMF}$ consistent with the lensing, dependent on the specific assumptions when separating the dark and baryonic mass, overall the lensing data are consistent with a relatively dwarf-poor IMF for SNL-1 (Newman et al. 2017).

Conversely, flexible spectral-fitting techniques applied to optical absorption spectra of SNL-1 require IMFs which are overabundant in dwarf stars (Newman et al. 2017). Not only is there a tension between

★ E-mail: adriano.poci@physics.ox.ac.uk

Table 1. Physical properties of SNL-1.

Redshift	z	0.0312	Smith et al. (2015a)
Einstein radius	$R_{\rm Ein}$	2.38 arcsec 1.48 kpc	Smith et al. (2015a)
Total mass	$\log_{10}(M/{\rm M}_\odot)$	10.98	Collier et al. (2018a)
Distance	D^a	132 Mpc 128 Mpc	Luminosity Angular diameter
Effective radius	$R_{\rm e}^{F814W}$	3.49 arcsec 2.15 kpc	Poci & Smith (2022)

[a]Derived from the redshift for our assumed cosmology.

these methodologies, then, but it is especially difficult to reconcile the fact that the spectroscopic results favour heavier populations than inferred by the dynamics (even with its DM uncertainty). SNL-1 therefore represents an interesting test case on which to refine these modelling techniques in order to ascertain the cause of this IMF discrepancy.

We have previously modelled spatially resolved integral-field unit (IFU) data of SNL-1 from Very Large Telescope (VLT)/Multi-Unit Spectroscopic Explorer (MUSE), taken in the Wide-Field Mode (WFM). From the dynamical model in that work (Poci & Smith 2022), SNL-1 appears to be considerably rotationally supported despite its global morphology and high velocity dispersion. There was evidence of mild triaxiality and mostly isotropic stellar orbits. That work also reaffirmed the high degree of compactness of SNL-1. One pertinent result from that model was that the dynamics and lensing, when computed independently of one another, show excellent agreement in the enclosed mass. We can hence consider the constraints from lensing and dynamics as consistent, to be contrasted with the discrepant spectroscopic results.

In this work, we explore the central region of SNL-1 using new high-resolution data – some of the highest physical resolution stellar kinematics published to date for a galaxy outside the Local Group. We aim to characterize the dynamics and populations using an array of sophisticated modelling techniques in order to understand how the different mass components are distributed. Ultimately, we aim to discern the cause of the tension between the different modelling techniques and measure the intrinsic IMF of SNL-1. Throughout this work, we assume a *Planck* 2018 cosmology (Planck Collaboration VI 2020), with $H_0 = 67.66\,{\rm km\,s^{-1}\,Mpc^{-1}}$ and $\Omega_{\rm m} = 0.3111$.

2 DATA AND TARGET

In this work, we present new observations of a well-studied, relatively nearby strong-lens galaxy SNL-1. The physical properties of SNL-1 are summarized in Table 1. SNL-1 is acting as a strong lens to a background source galaxy at $z = 0.926$; the lens modelling and results are described in detail in Smith et al. (2015a) and Collier et al. (2018a). This galaxy has been studied in the context of the stellar IMF thanks to the robust enclosed-mass constraints provided by the lensing (Newman et al. 2017). Despite being a massive ETG, the lens model results in a $M_\star/L = 4.61 \pm 0.39$ which is consistent with a Milky Way (MW)-like IMF (Kroupa 2002). In stark contrast, spectral analyses of this galaxy imply heavily dwarf-rich stellar populations, consistent with galaxies of similar morphology and central velocity dispersion.

2.1 Spectroscopy

With this work, we present new MUSE (Bacon et al. 2010) observations in the Narrow-Field Mode (NFM) with adaptive optics (AO; Arsenault et al. 2008; Ströbele et al. 2012) under program ID 109.22X3.001. The NFM of MUSE has a field of view (FoV) of 7.5 arcsec, sampled with 0.025 arcsec pixels. The spectral range is 4800–9300 Å, with a notch filter across 5780–6050 Å to block reflected light from the lasers of the laser tomography AO system. SNL-1 was observed in six Observing Blocks (OBs), each with a different dithering pattern and separate off-source sky frames, with a total on-source integration of 14 973 s. The raw frames were reduced by the standard ESO pipeline. Fig. 1 shows *Hubble Space Telescope* (*HST*) $F814W$-band photometry of SNL-1 from Smith et al. (2015a), overlaid with the footprint of the MUSE NFM.

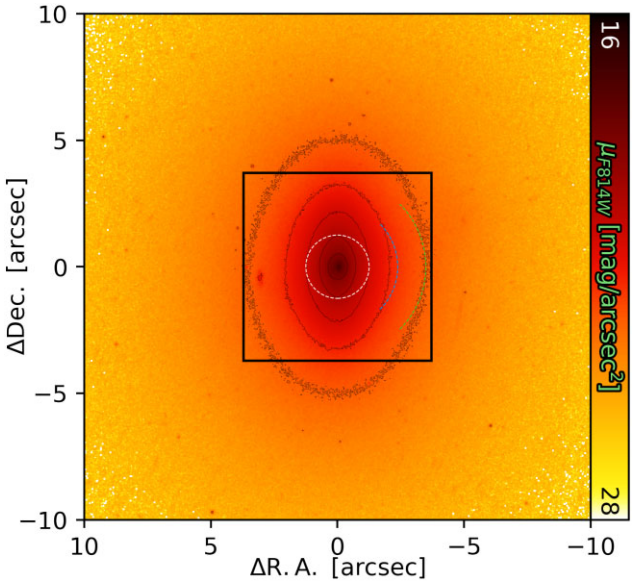

Figure 1. *HST* $F814W$ image of SNL-1. Isophotes are shown as thin black lines. The solid black box shows the FoV of the MUSE NFM. The dashed white circle has a diameter of 1.25 arcsec, which is the region explored in this work. The blue and green dashed arcs demarcate $R_{\rm Ein}$ and $R_{\rm e}$, respectively. SNL-1 exhibits flattened isophotes, though the effect of the dust lane is visible in the innermost contour.

The small pixel scale of NFM data results in significant readout noise, meaning that the signal-to-noise ratio (S/N) of the source drops off rapidly from the centre. Combined with some sky-subtraction issues in the data (see Appendix A), we choose to analyse the NFM data only in the brightest region. The high signal in this region means that those pixels are robust against sky-subtraction peculiarities, as well as requiring less spatial binning to reach the high S/N used in our analysis. It is also the critical region of interest, and one which is uniquely resolved by the NFM. Thus, we exclude all data outside of a circular aperture with diameter ∼1.25 arcsec (∼805 pc) centred on the brightest pixel. Regions outside this aperture are resolved by other data sets, such as the MUSE WFM in Poci & Smith (2022). A joint analysis will be explored in a forthcoming work.

The point spread function (PSF) of the NFM case is complicated by the use of the AO system. Such systems are generally expected to be characterized by a superposition of two Moffat profiles; one describing the corrected core, and one to account for the uncorrected natural seeing (e.g. Fétick et al. 2019). Since our target covers the full FoV of the NFM, we cannot estimate the PSF from the science observations as there are no isolated stars in the field. Thus, we have

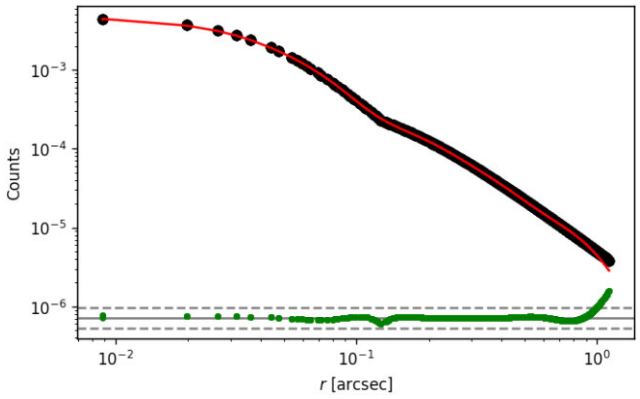

Figure 2. One-dimensional azimuthally averaged brightness profile of the model PSF. Black points show the PSF 'image' (the model provided by the MUSE ETC). The red solid line shows the MGE model fit to that image. The green points show the residuals of the fit (image − model/image), arbitrarily offset for presentation. The grey solid and dashed lines show the 0 and ±10 per cent (on a linear axis) of the residuals, respectively.

Table 2. PSF MGE model for the NFM observations, showing the normalized amplitude (left) and width (right) of each Gaussian. The model is normalized such that $\sum f_j = 1$ for j MGE Gaussians. We fit a circular PSF model, and so the Gaussian components all have an axis ratio of 1.

$\bar{f}$	σ (arcsec)	FWHM (arcsec)
0.4239	0.0219	0.0516
0.5045	0.0434	0.1022
0.0445	0.1104	0.2600
0.0216	0.2107	0.4962
0.0055	0.5392	1.2698

instead estimated the PSF by fitting a model to the predicted PSF from the MUSE exposure time calculator (ETC).[1]

The PSF was requested under the observational set-up used in Phase 2; namely, with a maximum airmass of 1.5.[2] The NFM AO performance depends sensitively on airmass, ambient seeing, and atmospheric coherence time (MUSE manual v12.1). Our six observations were acquired over three nights at low airmass (1.04–1.26, median 1.07), with good seeing (0.42–0.76 arcsec, median 0.49 arcsec) and coherence time (3.5–7.4 ms, median 5.5 ms). According to the MUSE manual v12.1, figs 37–39, these conditions are usually sufficient to yield close to the optimal delivered PSFs, and hence we expect that adopting the ETC model should not be an unreasonably optimistic assumption.

We chose to evaluate the PSF at a reference wavelength of $\lambda_{\rm ref} = 6500$ Å, as a compromise over the full spectral range from which we measure the stellar kinematics (Section 3). We fit a multi-Gaussian expansion (MGE) model (Cappellari 2002) to the PSF image. This is because not only is MGE general enough to accurately reproduce a double Moffat profile expected for the NFM PSF, but also because this parametrization is used later by our dynamical modelling implementation (Section 3.1). The PSF fit is shown in Fig. 2, and the model is tabulated in Table 2.

[1] https://www.eso.org/observing/etc/bin/gen/form?INS.NAME=MUSE + INS.MODE = swspectr

[2] The model for the NFM PSF from the MUSE ETC does not currently depend on the turbulence, and thus neither does our modelled PSF.

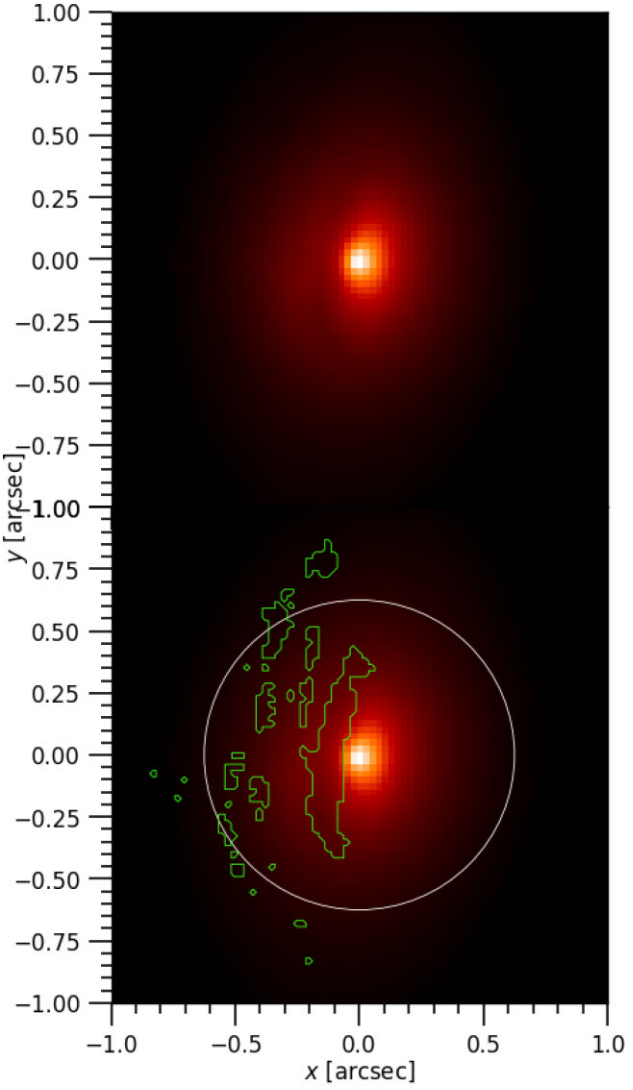

Figure 3. Top: Synthetic *HST* $F814W$-band image of SNL-1. Multiple dusty structures are visible on the near side SNL-1. Bottom: Identical image as above, but with the derived mask overlaid in green showing where dust has been detected, and subsequently removed. Overlaid in white is the circular FoV over which the spectroscopy is analysed in this work.

At the angular diameter distance of SNL-1, 1 arcsec ≈ 0.6 kpc. Accounting for the PSF, where the vast majority of the weight of the PSF core is $\lesssim$0.06 arcsec, these observations have an effective resolution of ∼36 pc. Hence, even the restricted aperture we have imposed is resolved by ∼20 resolution elements (PSF cores) across.

2.1.1 *Non-stellar features*

The NFM data show attenuation of the stellar light by dust. Nuclear bifurcated dust lanes are clearly seen in the white-light (spectrally integrated) data cube. The smallest resolved dust structure, in a clear disc/ring morphology, has an approximate radius of 0.4 arcsec (260 pc). Another dust structure is seen only on the approaching side of the galaxy (at least down to the depth of these data), extending out to ∼2 arcsec (1.3 kpc) in an arc. Fig. 3 shows a synthetic $F814W-$band image from the NFM data cube, scaled to highlight the central dusty ring structure. We mask the dust lanes henceforth since both the stellar population and kinematic

measurements could be biased in those sightlines. The masking of dusty pixels was done in the following way. First, a synthetic *HST* Wield-Field Camera 2 $F439W - F814W$ colour image was constructed to maximize contrast of the dust lane within the MUSE wavelength range. This was achieved by applying the respective filter curves directly to the spectra of the NFM data cube, then taking the difference. The synthetic colour image was then unsharp masked using a Gaussian filter with a kernel of 1.5 pixels. From that unsharp-masked image, all pixels below a threshold of 290 were assigned to the mask. This value was chosen to conservatively include all the foreground dust-obscured regions.

3 CENTRAL STELLAR KINEMATICS AT PARSEC-SCALE RESOLUTION

The central regions of ETGs have been of interest in galaxy-evolution studies for decades, believed to host a plethora of interesting and still-debated astrophysical processes. The central region of SNL-1 appears to be especially interesting even in the context of similarly massive ETGs. The rotation in SNL-1 (visible already from the long-slit data of Newman et al. 2017 and the MUSE WFM; Poci & Smith 2022) is unusually high given its morphology and mass. In this section, we look at measuring stellar kinematics at the high spatial resolution afforded by the NFM to study how the centre of this galaxy is gravitationally supported.

Before fitting the spectra to measure the kinematics, we spatially bin the data cube using a PYTHON implementation[3] of the Voronoi binning algorithm (Cappellari & Copin 2003) to a target S/N = 40. This S/N allows us to take advantage of the high spatial resolution of the NFM, while still being sufficient to measure non-Gaussian shapes of the line-of-sight velocity distribution (LOSVD). We consider the full rest-frame spectral range of MUSE covering $\lambda \in [4750, 9000]$ Å. We mask inadequately treated telluric features over the range [7600, 7700] Å, with an additional mask over the range [5700, 6100] Å to account for the notch filter of the AO system.

Stellar kinematics were measured using the PPXF PYTHON package[4] (Cappellari & Emsellem 2004; Cappellari 2017), and with the X-Shooter Stellar Library (XSL; Verro et al. 2022) in order to cover the full MUSE wavelength range. The library spectra were convolved with the wavelength-dependent line spread function (LSF) of MUSE prior to fitting. To robustly characterize the absorption-line shapes, and thus the LOSVD, a third-order additive polynomial was used during fitting, while a third-order multiplicative polynomial was included to account for low-frequency continuum mismatch. The LOSVD in each spatial bin is parametrized by four Gauss–Hermite coefficients (van der Marel & Franx 1993), approximately its mean velocity, velocity dispersion, skewness, and kurtosis, respectively. The measured kinematics can be seen in the left column of Fig. 5.

The NFM covers the high-rotation region, which was known from the WFM, which exhibits a maximum amplitude of $\pm 245\,\mathrm{km\,s^{-1}}$ within 3 kpc. However, in the NFM, the rotation extends further towards the centre than was previously seen, and becomes more confined to the major axis plane, in contrast to the dynamically hotter large-scale rotation. Combined with the dust geometry, this is strong evidence of a nuclear stellar disc, which is cospatial with the dust and ionized gas discs (Section 5). In the stellar component, this disc exhibits a maximum rotation amplitude of $\pm 165\,\mathrm{km\,s^{-1}}$ within 260 pc. We present pseudo-slit profiles of the stellar velocity and velocity dispersion in Fig. 4. This figure also reiterates that SNL-1 is pressure supported; the $|V|/\sigma$ can be read directly from Fig. 4 as ∼0.5.

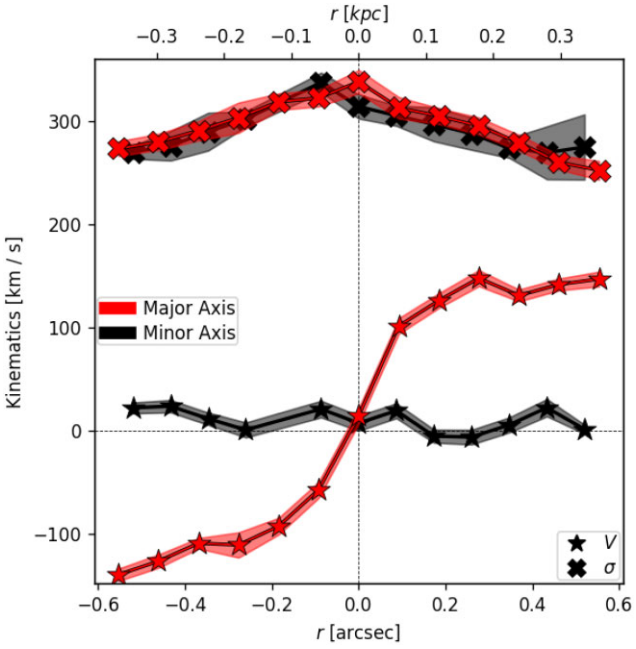

Figure 4. Pseudo-slit profiles of the stellar velocity (star symbols) and velocity dispersion (cross symbols) for SNL-1. The profiles are extracted within pseudo-slits laid on the binned kinematic FoV (S/N = 40) with a width of ±0.2 arcsec. Profiles are shown for major-axis (red) and minor-axis (black) slits. Shaded regions illustrate the mean measurement uncertainty of the kinematic fits in each region.

3.1 Orbital dynamical models

We employ highly general triaxial Schwarzschild orbit-superposition models (Schwarzschild 1979; van den Bosch et al. 2008) in order to understand the internal structures which give rise to the new observed kinematics. We have already fit Schwarzschild models for SNL-1 (Poci & Smith 2022) to the WFM, though we were unable to confidently disentangle the mass components in the centre due to the relatively large PSF. With a dynamical model of the new kinematics, we aim to break the degeneracy of the central mass composition, since the central supermassive black hole (SMBH) is dynamically resolved by these data.

Briefly, the Schwarzschild models integrate, for a given gravitational potential, a large library of stellar test orbits which are permitted to reside in said potential. From this library, the optimal subset is fit in order to most accurately reproduce the observed stellar kinematics. This entire process is repeated for many choices of intrinsic (deprojected) gravitational potentials, which are all consistent with the observed (projected) stellar mass distribution. We take the model with the best goodness-of-fit measure and the corresponding best-fitting subset of orbits to represent the intrinsic mass distribution and stellar kinematics of the galaxy.

The model we use for the projected mass distribution (in order to sample plausible intrinsic gravitational potentials) is derived by fitting an MGE (Cappellari 2002) to the *HST* $F814W$ photometry. By using the stellar light to model the projected mass, we implicitly assume that the $M_\star/L$ is spatially constant (over the small FoV of the kinematics). We explore the impact of this assumption in a

[3] Available at https://pypi.org/project/vorbin/.
[4] Available at https://pypi.org/project/ppxf/.

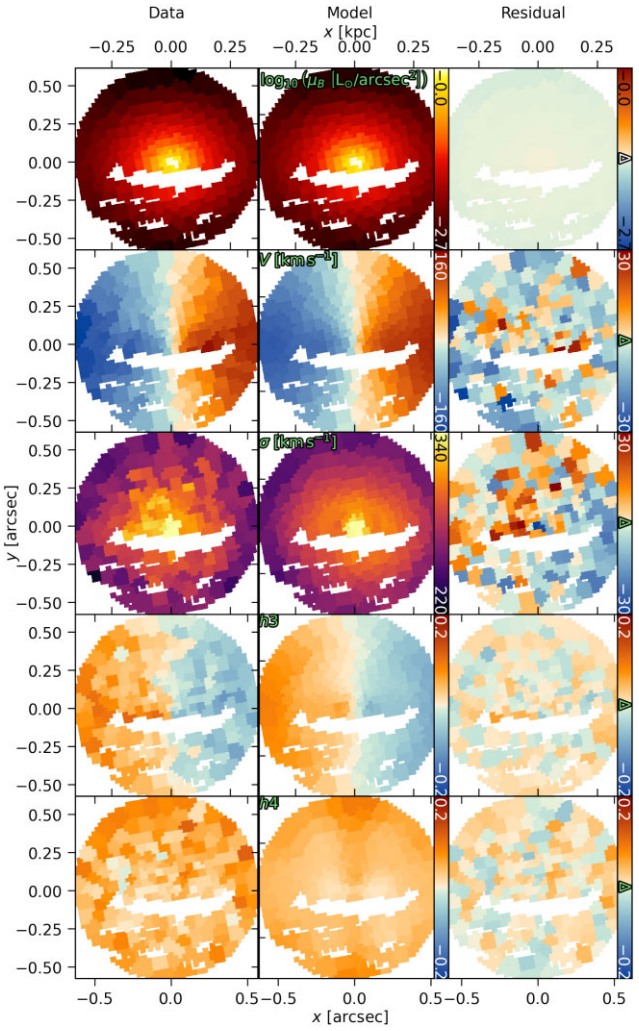

Figure 5. The measured stellar kinematics (left), the corresponding best-fitting Schwarzschild model (centre), and the residuals (data − model; right) for the NFM data of SNL-1. The rows from top to bottom show the projected surface brightness, rotational velocity, velocity dispersion, h_3, and h_4.

forthcoming work. In the general case, the intrinsic gravitational potentials are characterized by seven free parameters:

(i) the mass of the central SMBH, $M_\bullet$;
(ii) the axis ratios of the intrinsic mass distribution, q, p, u, where $q = C/A$, $p = B/A$, and $u = A'/A$, for major, intermediate, and minor axes A, B, and C, and projected major axis A';
(iii) parameters of the Navarro–Frenk–White (Navarro, Frenk & White 1996) cold DM halo, the concentration $C_{\rm DM}$, and mass fraction at r_{200}, $M_{200}/M_\star$;
(iv) a spatially constant $M_\star/L$ scale factor, Υ.

In this work, due to the restricted FoV of the stellar kinematics, we do not attempt to fully constrain the DM halo, but instead tie the two parameters together using the concentration–mass relation of Dutton & Macciò (2014), so that in practice, we sample only $M_{200}/M_\star$ and are therefore reduced to six free parameters.

The implementation of the Schwarzschild model used in this work samples three conserved integrals-of-motion which are, in a triaxial potential, the energy E, a non-analytic z-axis angular momentum I_2, and a third non-classical conserved integral I_3. We sampled E, I_2, and I_3 in 30 logarithmic, and 25 and 18 linear steps, respectively, generating a library of tube orbits. The same set-up was used to generate a separate library of box orbits. We applied a dithering to this orbital sampling of a factor of 3 (in each integral; 3^3 in total). For every starting coordinate in the integral-of-motion space, this dithering samples three slightly perturbed coordinates in each dimension, producing a 'cloud' of orbits around each point, and reducing discreteness in the orbit library.

At every iteration, the model 'observables' were first spatially binned and convolved with the PSF of the NFM observations in order to be directly comparable to our measured stellar kinematics. We then defined the best-fitting model as that which has the minimum χ^2 across all four Gauss–Hermite kinematic moments. The best-fitting Schwarzschild model is shown in the middle column of Fig. 5, with the residuals (data − model) in the right column. The exploration of the model parameters is shown in Fig. 6. Models are coloured by their goodness-of-fit, relative to the best-fitting model, as

$$\left[\chi^2_{\rm r} - \min(\chi^2_{\rm r})\right] / \sqrt{2 N_{\rm obs} N_{\rm GH}} \tag{1}$$

for the number of Voronoi bins, $N_{\rm obs} = 179$, the number of Gauss–Hermite kinematic moments fit in the Schwarzschild model, $N_{\rm GH} = 4$, and χ^2_r as defined in Zhu et al. (2018) and Poci et al. (2019). Fig. 6 indicates that the constraints on the DM are weak, as might be expected given that the data cover only the most baryon-dominated region. Conversely, we see that the constraints on the SMBH mass are much more secure. The best-fitting SMBH mass is $M_\bullet = \left(1.62^{+0.056}_{-0.054}\right) \times 10^9\,{\rm M}_\odot$. Despite the grid-based approach to our parameter sampling, we still resolve the $M_\bullet$–$\Upsilon_\star$ anticorrelation. Fig. 7 shows the impact of changing $M_\bullet$ on the stellar kinematics.

From Fig. 5, the model is able to reproduce all the measured moments of the LOSVD to a high degree of accuracy. The physical properties of the best-fitting model are given in Table 3. The dynamical model suggests an inclination of 65°, which implies that the intrinsic thickness of the nuclear disc is thinner still than what appears in projection in the kinematic maps. Indeed, we find a remarkably flattened structure in the central region. This is perhaps expected, given the high degree of ordered rotation, but it is atypical for galaxies of this mass and global morphology. The minor-to-major axis ratio C/A becomes as flat as ∼0.5 towards the edge of the FoV. Fig. 8 presents the axis ratios as a function of radius. It clearly illustrates that the nuclear disc is truly a distinct structure, since at both smaller and larger radii, SNL-1 is more spherical than in this region (∼0.4 arcsec/260 pc). The origin of this disc, though discussed further below, remains unclear. However, ongoing work with multiple tracers (including ionized and molecular gas) aims to solve this puzzle.

The Schwarzschild model provides a measure of the intrinsic dynamical support within SNL-1. Fig. 9 shows the orbital circularity from the fit to the NFM kinematics, defined in Zhu et al. (2018), and given here in equation (2):

$$\lambda_z = \overline{L_z} / \left(\overline{r}\,\overline{V_2}\right), \tag{2}$$

with

$$\overline{L_z} = \overline{x V_y - y V_x},$$
$$\overline{r} = \overline{\sqrt{x^2 + y^2 + z^2}},$$
$$\overline{V_2}^2 = \overline{V_x^2 + V_y^2 + V_z^2 + 2V_xV_y + 2V_xV_z + 2V_yV_z}.$$

The orbital circularity is a normalized measure of the vertical angular momentum. According to this definition, $\lambda_z = 1\,(-1)$ corresponds to corotating (counter-rotating) disc orbits, while $\lambda_z = 0$ corresponds

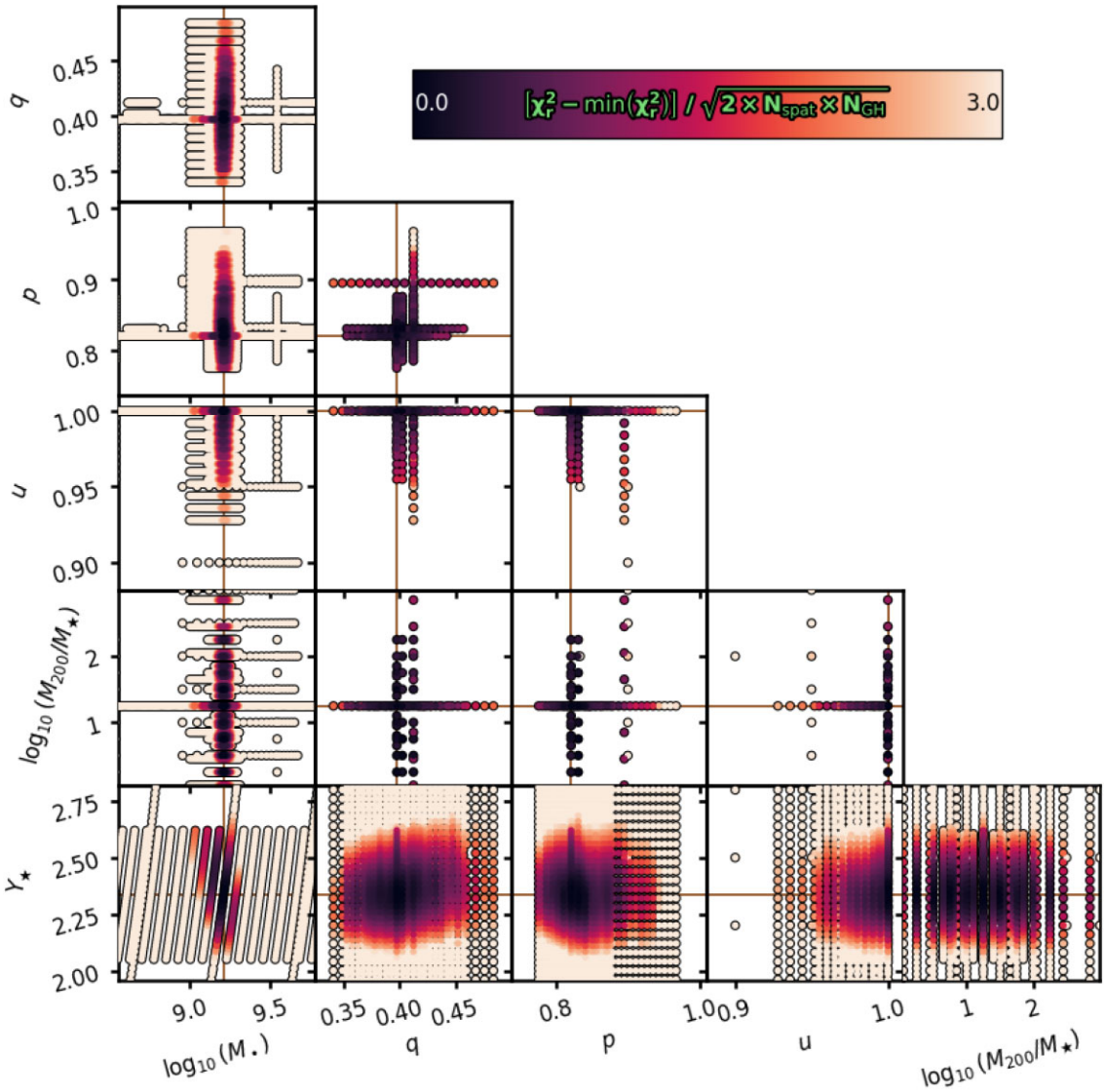

Figure 6. Subset of the parameter exploration for the Schwarzschild model of SNL-1. Points are coloured by relative goodness-of-fit as given by equation (1). Best-fitting parameters are demarcated by solid brown lines. The panels show a subset of the total parameter space explored, focusing on the low χ^2 region. The full parameter-space exploration is shown in Appendix C.

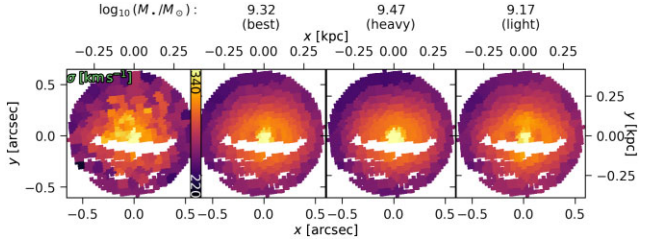

Figure 7. Impact of changing the SMBH mass on the predicted stellar velocity dispersion. From left to right are the measured kinematics, the best-fitting model, a model with an overmassive $M_\bullet$, and a model with an undermassive $M_\bullet$, given by adjacent steps in the parameter space. The other parameters of the model are held fixed at the best-fitting values. The impact of changing $M_\bullet$ is seen clearly in the velocity dispersion, where the central peak is visibly overpredicted and underpredicted for the overmassive and undermassive models, respectively.

Table 3. Free parameters of the Schwarzschild model, their best-fitting values, and the associated uncertainties. Uncertainties are derived by taking the spread of parameter values of all models within 1σ of the best-fitting solution, which is visualized in Fig. 6. Note that θ', ϕ', ψ' are derived from the best-fitting q, p, u, while $C_{\rm DM}$ is computed from $M_{200}/M_\star$ (Section 3.1).

Parameter	Description	Best	1σ
$\log_{10}(M_\bullet/\mathrm{M}_\odot)$	Black hole mass	9.21	0.0148
q	Intrinsic shape	0.3973	0.0135
p	Intrinsic shape	0.9210	0.0156
u	Intrinsic shape	0.9999	0.0042
θ'	Viewing angle	65.00°	
ϕ'	Viewing angle	89.26°	
ψ'	Viewing angle	89.26°	
$C_{\rm DM}$	DM concentration	7.6211	–
$\log_{10}(M_{200}/M_\star)$	DM ratio at r_{200}	1.2500	0.2850
Υ ($\mathrm{M}_\odot/\mathrm{L}_\odot$)	Global M/L	2.335	0.0753

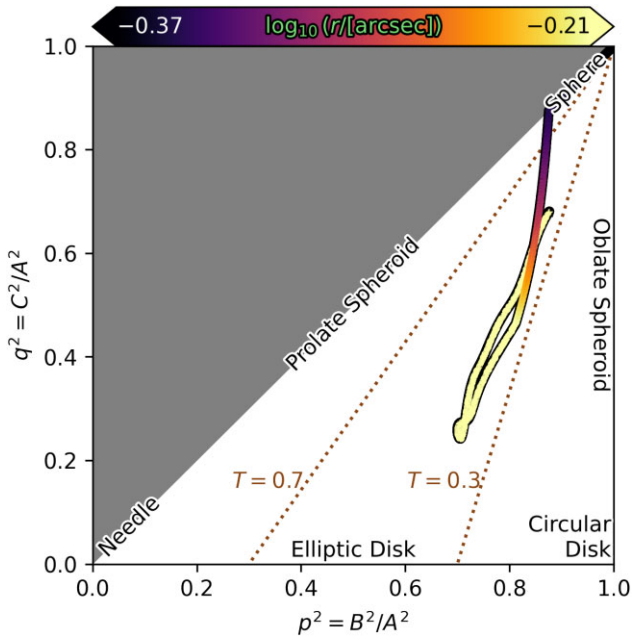

Figure 8. Minor-to-major axis ratio q against intermediate-to-major axis ratio p, as a function of radius. The left and right extrema of the colour bar denote the full width at half-maximum of the PSF and maximum extent of the kinematics, respectively. The model extends beyond these bounds, but is unconstrained by the spectroscopy in those regions.

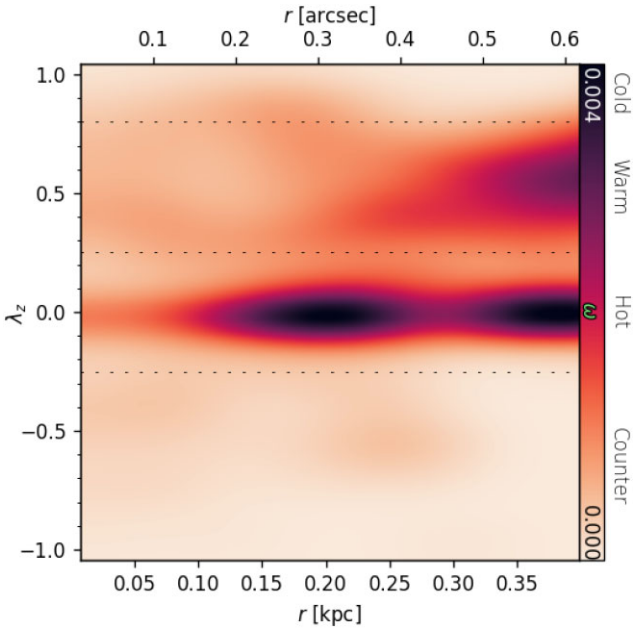

Figure 9. Orbital circularity λ_z as a function of time-averaged mean orbital radius, for the best-fitting Schwarzschild model. Darker colours indicate higher contributions to the model. Horizontal dashed lines demarcate the orbital categories defined in Zhu et al. (2018), with corresponding labels on the right.

to dynamically hot/box/chaotic orbits. The peaks in the circularity distribution in Fig. 9 can be linked to the structures already identified in the kinematics. A heavily pressure-supported component is clearly seen at $\lambda_z = 0$, which dominates the mass budget. There exists a weak peak at high circularity ($\lambda_z \approx 1$) and small radius ($r \approx 0.15$ kpc), which represents the nuclear disc. A warmer component ($\lambda_z \approx 0.5$) begins to emerge towards the edge of the FoV, which was found in Poci & Smith (2022) to be responsible for the larger-scale rotation seen in the WFM.

The limited extent of the NFM data might result in the under-population of particular orbital families in the Schwarzschild model (e.g. Krajnović et al. 2008). While in this work we do not attempt to combine the NFM and WFM kinematics, we can broadly compare the individual model outputs, though some are not directly comparable. We also re-emphasize here that there is no spatial overlap between the two data sets, so direct quantitative comparisons would require an extrapolation in one direction. From the NFM model, we found $(q, p, u) = (0.3973, 0.9210, 0.9999)$, compared to the WFM model with $(q, p, u) = (0.4949, 0.8390, 0.9910)$. This indicates a preference for rounder shapes in the WFM, but mild triaxiality in both. The models in fact independently predict that the central region, around the extent of the nuclear disc, is flatter than the outskirts. Given this region is unresolved in the WFM, it would naturally result in a thicker average intrinsic shape. The comparison of the parameters of the DM halo is not as straightforward. For the NFM, we do not expect to constrain those parameters, and thus decided to couple $C_{\rm DM}$ and $\log_{10}(M_{200}/M_\star)$. In the WFM model, these parameters could vary independently. We find that the NFM model predicts a smaller fraction of DM even at fixed radius compared to the WFM model. The comparison of $\Upsilon_\star$ is also not trivial, since the WFM model included spatially varying $M_\star/L$ during the construction of the gravitational potential, which renormalizes the output $\Upsilon_\star$.

We can instead compare the total masses predicted by the models at fixed radii. The NFM model produces an enclosed stellar mass of $\log_{10}\left[M_\star(<1\,\text{kpc})\right] = 10.65$ (emphasizing that this is an *extrapolation* beyond the NFM data), while the WFM model produces $\log_{10}\left[M_\star(<1\,\text{kpc})\right] = 10.77$. Similarly, the total enclosed masses are $\log_{10}\left[M_{\rm dyn}(<1\,\text{kpc})\right] = 10.67$ and $\log_{10}\left[M_{\rm dyn}(<1\,\text{kpc})\right] = 10.81$ for the NFM and WFM models, respectively. Thus, instead of the multiscale model, we conclude that the NFM model alone is not significantly biased in the physical properties we analyse in this work.

4 CENTRAL STELLAR POPULATIONS AT PARSEC-SCALE RESOLUTION

Spectroscopic IMF measurements are often reported to become dramatically more dwarf-rich towards the centres (within the central ∼1 kpc) of similar galaxies (e.g. La Barbera et al. 2017, 2019; Martín-Navarro et al. 2021). SNL-1 exhibits similarly dwarf-rich spectral signatures in its centre (Newman et al. 2017), though a radial gradient analysis has not been conducted. We seek here to conduct such a radial investigation and to understand if the new NFM data could potentially resolve the IMF discrepancy, or reaffirm the peculiar nature of the stellar populations in SNL-1.

4.1 Generalized full spectral fitting

To be able to measure the IMF directly in the centre of SNL-1, we employ a highly flexible spectral-fitting code known as the Absorption Line Fitter (ALF; Conroy et al. 2018). ALF uses the extended MILES+Infrared Telescope Facility empirical single stellar population (SSP) library (Villaume et al. 2017) to fit for stellar kinematics, ages, 19 individual elemental abundances, and the stellar IMF. ALF uses a FORTRAN version of the EMCEE package (Foreman-Mackey et al. 2013) to sample the posterior distribution of its large parameter space, which includes the physical parameters mentioned

above, as well as a number of technical nuisance parameters to account for instrument artefacts and atmospheric corrections.

This kind of fitting is highly demanding on the input spectra, and so for our restricted FoV, we rebin the data cube to a target S/N = 80. Although this sacrifices some spatial resolution, it is necessary to robustly constrain the highly flexible fits of ALF. We still resolve the new FoV with 10 spatial bins across. Given the specific aims and data quality of our observations, we run a non-standard fitting set-up of ALF. We do not fit all 19 elemental abundances for every spatial bin, given that even the increased S/N may not be sufficient to constrain them all simultaneously. Instead, we first construct an aperture spectrum by integrating over the circular FoV we derived earlier (still masking the dusty pixels to avoid a biased spectrum). We fit this single spectrum with the full flexibility of ALF. The results of the fit are then used to fix many of the elemental abundances when we subsequently fit the individual binned spectra. In this way, we limit the flexibility of ALF while retaining the ability to directly measure the IMF. Namely, we fix the elemental abundances of [Si/H], [K/H], [V/H], [Cr/H], [Mn/H], [Co/H], [Ni/H], [Cu/H], [Sr/H], [Ba/H], and [Eu/H] to the best-fitting values (maximum likelihood of the posterior distributions) derived from the full fit to the aperture spectrum. We opt to keep the abundances of [O/H], [C/H], [N/H], [Na/H], [Mg/H], [Ca/H], and [Ti/H] free, as these have a more direct impact on the measured IMF, and have been measured in some galaxies to have significant gradients (e.g. La Barbera et al. 2019, 2021; Parikh et al. 2024). The results of the aperture fit are shown in Appendix D.

In both runs of ALF, the IMF is parametrized as a two-part broken power law, defined by the slopes α (a free parameter) for $m_\star \in [0.08, 1.0)\,\mathrm{M}_\odot$, and $\alpha_{\mathrm{Salpeter}} = 2.3$ for $m_\star \in [1.0, m_{\mathrm{max}}]\,\mathrm{M}_\odot$. We leave the default $m_{\mathrm{max}} = 100\,\mathrm{M}_\odot$. To sample the posterior distributions, we run ALF with 1024 walkers. These walkers do 10 000 burn-in steps each, a further 10 000 burn-in after reinitialization, then a final 100 steps to sample the posteriors from which the best-fitting values are determined. Such a set-up is robust against local minima, and thoroughly searches the large parameter space. This scheme is used for both the integrated aperture and binned spectra.

4.2 Results

We present 2D maps for a number of properties of interest, generated using the maximum likelihood solution at every spatial location. The SSP-equivalent mean stellar age and mean stellar metallicity are shown in Fig. 10. These results cover a small dynamic range, and we see that the scatter between spatial bins is larger than any systematic gradient that may be present.

ALF also fits for the low-mass slope of the IMF directly. The top panel of Fig. 11 shows the measured α, describing the mass range $m_\star \in [0.08, 1.0)\,\mathrm{M}_\odot$. We see that, in agreement with Newman et al. (2017), the IMF slope across the region covered by the NFM is, on average, consistent with a Salpeter IMF, implying a high concentration of low-mass stars. But there is little other structure in the IMF map, especially with regard to radial gradients.

The corresponding $M_\star/L_{F814W}$ for the measured age, metallicity, and IMF slope is shown in the bottom panel of Fig. 11. The $M_\star/L$ should closely track the variations, or lack thereof, of the IMF map in the panel above. Small deviations can be caused by additional variations in the age and metallicity.

Finally, Fig. 12 shows maps of the remaining elemental abundances which are left free in our fits; namely, [O/H], [C/H], [N/H], [Na/H], [Mg/H], [Ca/H], and [Ti/H]. We see that there is no significant structure in any of these properties either, with the exception of the tentative evidence for gradients in [Na/H] and [N/H]. Moreover,

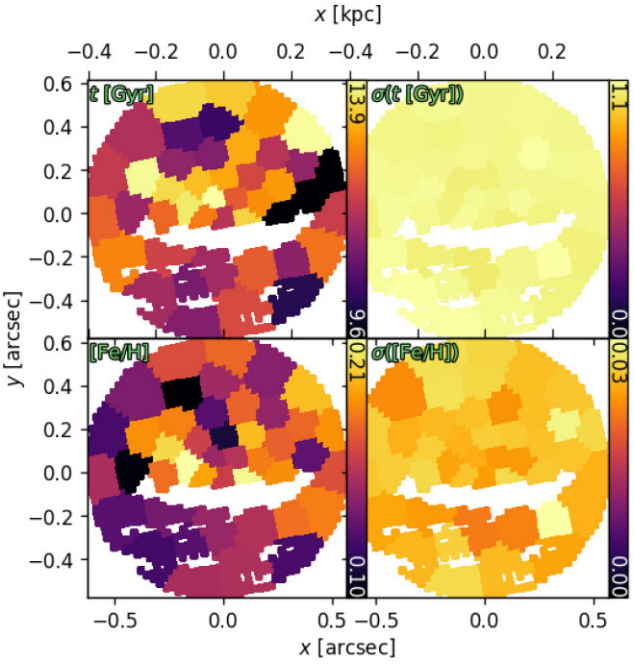

Figure 10. Left: SSP-equivalent mean stellar age (top) and mean stellar metallicity [Fe/H] (bottom) from ALF. Right: The corresponding 1σ uncertainties derived from the posteriors of the ALF fit to each Voronoi bin.

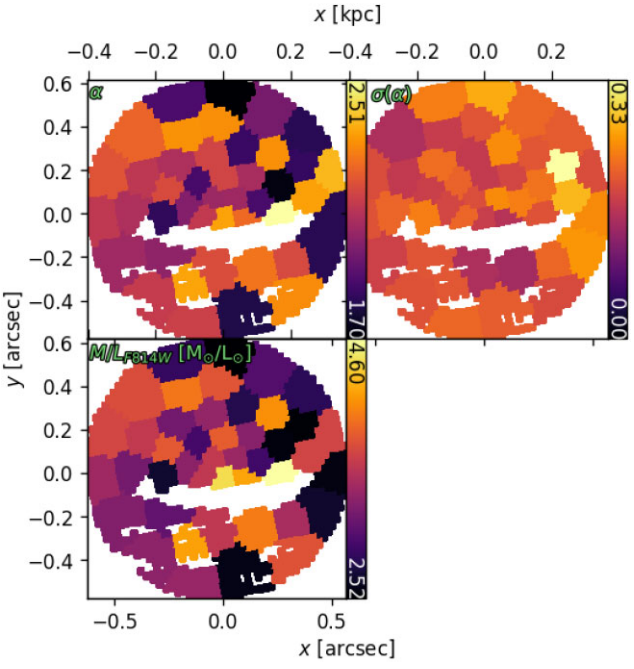

Figure 11. As Fig. 10, but for the low-mass slope of the IMF α (top) and $F814W$-band $M_\star/L$ (bottom). The $M_\star/L$ is derived from the outputs of ALF, rather than being fit directly on the spectra. It therefore has no posteriors.

the abundances of [O/H] and [Na/H] are markedly higher than the other elements.

For a more quantitative assessment of the presence of any gradients, we show radial profiles of all of these stellar population properties in Fig. 13. These profiles are computed by taking the median value within concentric elliptical annuli with the ellipticity of the stellar surface brightness MGE. Corroborating the expectation

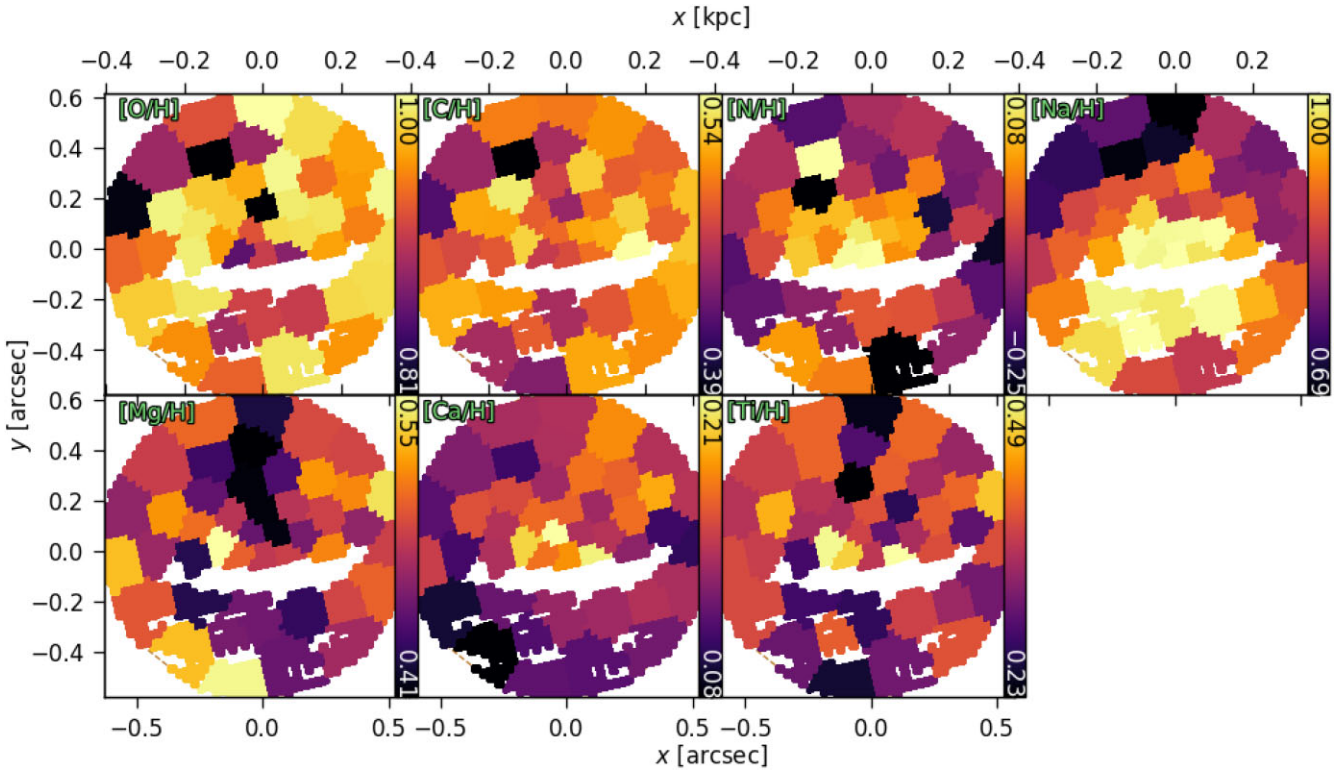

Figure 12. Elemental abundances as measured in ALF.

from the 2D maps, we recover flat gradients in the measured properties. These data, however, probe only the central ∼350 pc. This is interior to the typical transition radius of previous studies (1 kpc; e.g. La Barbera et al. 2017; van Dokkum et al. 2017). It is thus unclear how prevalent gradients on the spatial scales studied here are, although they have been observed with spectral indices in M31 on scales of ∼100 kpc (La Barbera et al. 2021).

We see that some spatial bins, especially near the dust mask, exhibit strongly double-peaked posterior distributions in some parameters. In addition, we select the maximum likelihood solution from the posterior, which can be slightly offset from the mode of the distribution for any finite number of Markov chain Monte Carlo (MCMC) samples. For these reasons, the randomly sampled curves in Fig. 13 sometimes deviate from the measured curve.

5 IONIZED GAS

In addition to absorption-line stellar properties, we measure emission-line ionized-gas kinematics from the new data cube. Because the ionized gas emission is faint compared to the starlight, we first fit and subtract a model for the stellar continuum using PPXF. The treatment here differs from the usage of PPXF in Section 3 for measuring stellar kinematics, since the appropriate smoothing scale for the gas will differ from that of the stars. We do not, in this case, need to measure reliable stellar kinematics, but rather reliably estimate the stellar continuum.

For every pixel in the central $1.25 \times 2.50\,\mathrm{arcsec}^2$ region of the cube, we extract a spectrum spanning 4680–7150 Å (rest frame) from a circular aperture with radius varying linearly from 0.05 to 0.30 arcsec, according to distance from the galaxy centre. We then mask the wavelength regions corresponding to the Hβ, [O III] 5007 + 4959, Hα, and [N II] 6548 + 6584 emission lines, regardless of whether emission is detected or not. This spectrum is then fit using simple stellar population spectral templates from Vazdekis et al. (2016), using multiplicative and additive polynomials of orders 10 and 1, respectively, to provide a high degree of flexibility. The resulting continuum model is subtracted from the single observed target pixel, thereby yielding a residual emission-line cube retaining the full spatial resolution of the original data as far as possible.

Fig. 14 shows position–velocity diagrams (PVDs) from the [NII] line. This fit was done by collapsing the continuum-subtracted cube onto pseudo-slits (given in the figure), then measuring the full LOSVD of the [N II] line profile at every position along the slit. This process allows for complexity in the gas kinematics, including, for instance, multiple cospatial kinematic components.

The PVDs reveal two distinct kinematic components: a sharply rising rotation at the centre, contributing only within about ±0.2 arcsec from the major axis, and a shallower component reaching to ∼2 arcsec. The resulting X-shaped structure is of a form commonly observed in barred galaxies, where it arises from gas trapped in orbital resonances (e.g. Athanassoula & Bureau 1999).

To extract a simple velocity field, we fitted the Hα + [N II] complex in the emission data cube with a three-Gaussian model. The three lines were constrained all to have the same LOSVD (cf. the PVD fits above), while the Hα and [N II] doublets have free amplitude (but the ratio between the [N II] line amplitudes is fixed). An important caveat to this is that the central regions of SNL-1 are not in fact well described by a single LOSVD, as may be expected from the complex PVD structure. We fitted the three-Gaussian model to spectra extracted from circular apertures centred on each pixel, with a range of sizes, implementing a crude adaptive smoothing scheme.

The fit started with an aperture of radius 0.400 arcsec (16 pixels) around the target pixel, and reduced the size by factors of 2, to a final radius of 0.025 arcsec (1 pixel). Each fitting step was initialized

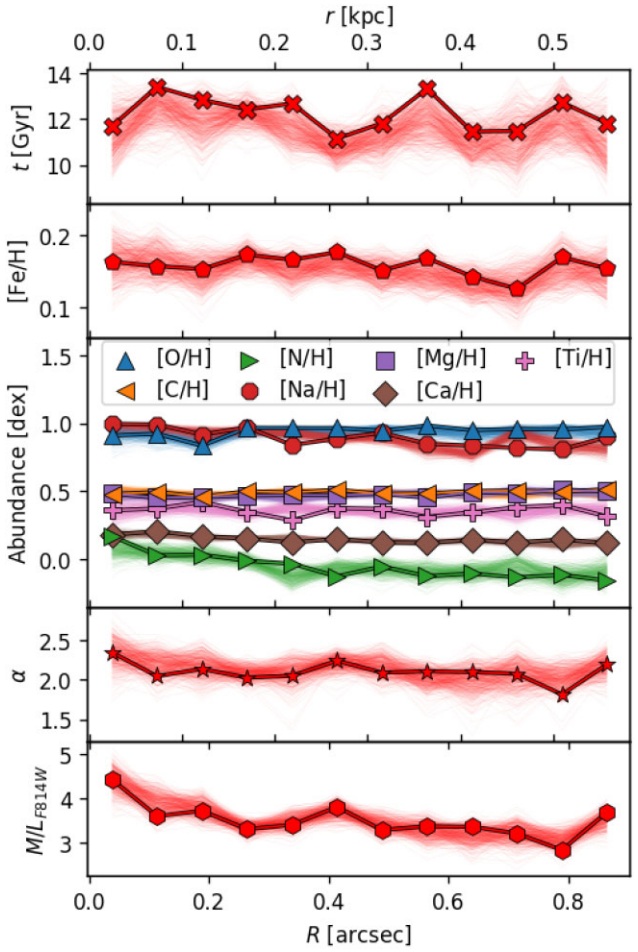

Figure 13. Radial profiles of a number of stellar population properties measured from ALF; from top to bottom, SSP-equivalent mean stellar age, stellar metallicity [Fe/H], the individual elemental abundances which were left free to vary, the low-mass IMF slope, and the $M_\star/L_{F814W}$. For every measured property, we recreated 2D maps by randomly sampling the posterior distributions of all spatial bins, and remeasured the radial profiles. This was repeated 500 times, and are shown as light curves in the background of each panel.

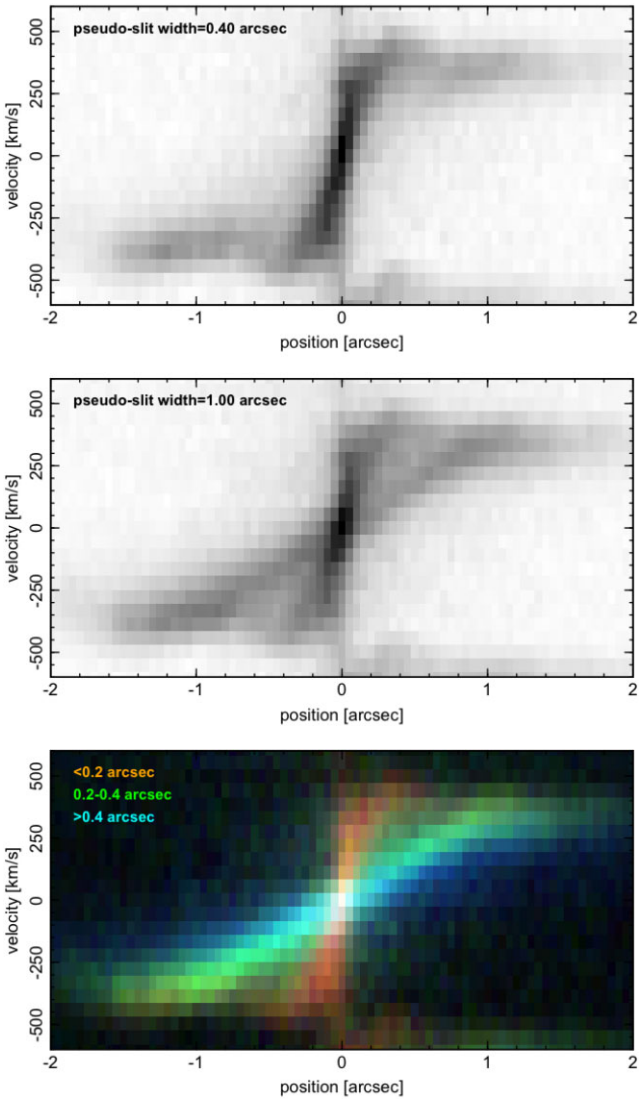

Figure 14. Major-axis PVDs for the [N II] 6584 Å line, for two different pseudo-slit widths (upper panels) and a colour rendering (lower panel) in which the red channel reproduces the upper panel, while green and blue show pixels further from the major axis. Contamination from the Hα line can be seen at the bottom right of each figure.

from the preceding (larger) aperture, to help avoid false minima at the smaller smoothing scales. The final velocity at each pixel is that obtained with the smallest aperture size yielding a peak S/N ratio S/N > 3. In practice, around 50 per cent of the map pixels have an effective smoothing smaller than the nominal PSF core, and pixels with larger smoothing are at larger radius where fine spatial structure is not expected.

The resulting velocity field is shown in Fig. 15, alongside the equivalent map derived from the lower resolution MUSE WFM data of Poci & Smith (2022), with *HST* images from Collier et al. (2018a) provided for context. On scales similar to the effective radius (∼3.5 arcsec) the WFM data confirm the presence of rapid major-axis rotation in the same sense as the stellar kinematics, while beyond ∼5 arcsec, the rotation continues but warps to a different position angle. The new NFM observations trace the rotation signature inwards to small scales, where it appears to peak at ∼0.4 arcsec (much larger than the nominal PSF core), corresponding to the inner structure already seen in the PVDs in Fig. 14. The isovelocity contours in the NFM region show some slight asymmetry, indicating deviation from circular motion (e.g. Spekkens & Sellwood 2007).

Finally, the integrated [N II] emission-line image is presented in Fig. 16, and shows that the emission surface brightness rises sharply inside the ±0.4 arcsec velocity peaks. A distinct spiral-like enhancement is clearly visible on the northern (approaching) side, at 0.6–1.2 arcsec from the galaxy centre. Such structures have been seen in ionized gas in spiral galaxies (e.g. Kam et al. 2015; Mitchell et al. 2015; Della Bruna et al. 2022; Emsellem et al. 2022), but few ETGs have been studied with this spatial resolution. Together, Figs 14–16 reveal complex structures in the inner regions of SNL-1, including features more associated with spiral and barred systems than with classical massive elliptical galaxies.

6 COMPARING SNL-1 TO THE GALAXY POPULATION

We detect no internal variations in most of the stellar population properties of SNL-1 over the small spatial region studied here.

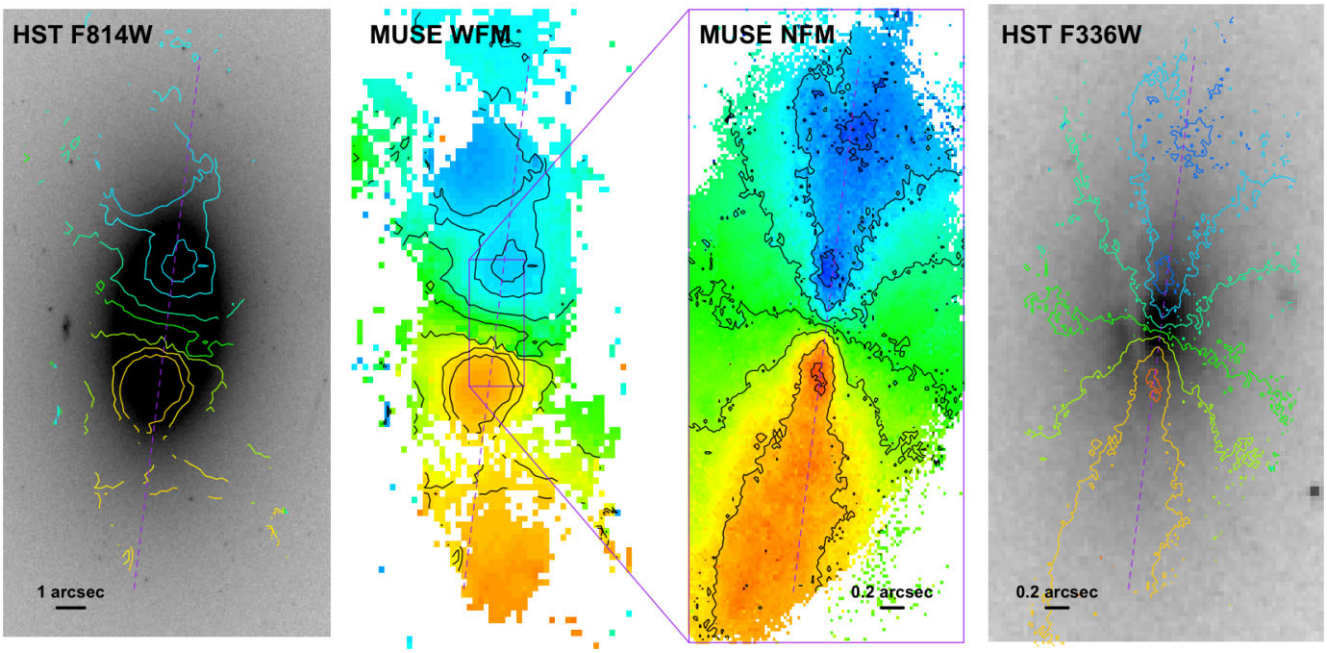

Figure 15. Gas velocities derived from the WFM and NFM observations. The leftmost panel shows the WFM velocities as contours overlaid on the *HST F*814*W* image, while the colour map in the next shows more clearly the extent of the gas measurements. The third and fourth panels show the inner structures derived from the NFM data, and a comparison to the *HST F*336*W*, respectively. In each pair of panels, the velocity contours are chosen to highlight relevant features; in the WFM they are drawn at 0, ±150, ±260, ±290 km s^{-1}, showing the global rotation and outer warp, while for NFM they are at 0, ±150, ±300, ±400 km s^{-1}, emphasising the fast-rotating inner disc. The purple dashed line in all panels is the stellar kinematic position angle as a guide.

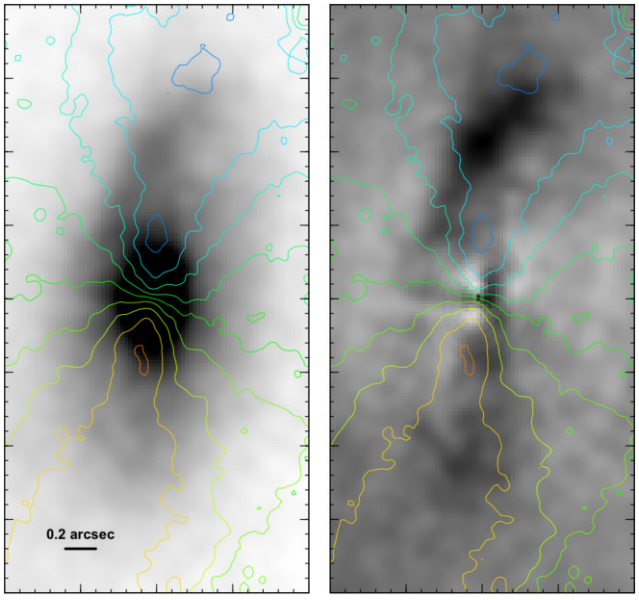

Figure 16. Left: Collapsed [N II] emission-line image (approximately corrected for Hα contamination), with velocity contours overlaid. Both fields have been smoothed to enhance visibility of the main structures. Right: The same after subtracting a simple elliptically symmetric model, highlighting the spiral features.

Although few comparable galaxies have been observed at this spatial resolution, it appears that other massive ETGs typically harbour stronger radial gradients. In particular, past works (e.g. Conroy, van Dokkum & Villaume 2017; La Barbera et al. 2017) have observed much more significant gradients in the 'IMF'. However, we emphasize that there are numerous differences between these past works, as well as our own, including the spatial resolution and extent of the data, the assumed functional form of the IMF, and what is measured by each 'IMF' parameter – over and above any intrinsic differences in the target galaxies of each work. Our NFM data are limited to the region, which is unresolved by the typical PSF of previous works. A joint, self-consistent analysis of multiscale data sets will ultimately be able to elucidate any gradients in SNL-1 specifically.

Where comparable, our spectral results are in some cases consistent with previous works, and in other cases show significant differences. Compared[5] to the previous work (Gu et al. 2022; Cheng et al. 2023; den Brok et al. 2024), the results for SNL-1 indicate that it sits at the metal-rich end of the samples studied in those works. In fact, many elements show especially good agreement with the brightest cluster galaxies sample of den Brok et al. (2024), including those which we only measure on the aperture spectrum (Appendix D). The exceptions are oxygen and sodium, which are substantially elevated in SNL-1. While modelling systematics may be playing a role here, especially in the regime of the extreme abundances measured, it is also difficult to compare disparate (and relatively small) samples of galaxies in such a detailed manner due to the possibility of substantial intrinsic scatter. In each of those past works, at most one galaxy from each sample has similar velocity dispersion to SNL-1, indicating that the physical properties and/or formation histories may also differ. Thus, while the abundances of oxygen and sodium are relatively

[5]Most previous works report elemental abundances with respect to iron, [X/Fe]. When comparing our results, therefore, we apply the straightforward conversion [X/Fe] = [X/H] − [Fe/H] ≈ [X/H] − 0.16 (the value from the aperture spectrum fit).

high compared to other available measurements, we cannot exclude the possibility that the abundances in SNL-1 are truly high.

More broadly, our models must be taken in light of the particular properties of SNL-1 in the context of the galaxy population as a whole. SNL-1 exhibits some unusual characteristics, further highlighted by our new NFM data. The stars in SNL-1 simultaneously exhibit a peak velocity dispersion of $\sim$350 km s^{-1} and peak rotation velocity of $\sim$250 km s^{-1} (at larger radii than shown here; Poci & Smith 2022). It is highly compact (Table 1), and morphologically appears to be a quintessential massive elliptical galaxy. In contrast, galaxies in the compact ETG samples of Deeley et al. (2023) and Grèbol-Tomàs, Ferré-Mateu & Domínguez-Sánchez (2023) do not reach that magnitude in velocity or velocity dispersion, much less both simultaneously. Only one object from the catalogue of compact galaxies of Spiniello et al. (2024) exceeds this velocity dispersion. Interestingly, from the parent sample of SNELLS, selected specifically to have high velocity dispersion, only three other galaxies reach a comparable magnitude (Smith et al. 2015a). Overall, therefore, SNL-1 occupies the high-velocity-dispersion tail of the galaxy population.

The star formation history[6] (SFH) of SNL-1 indicates that it assembled very early, and its stellar populations have remained largely unchanged since. The early and rapid SFH of SNL-1 is comparable to relic galaxies (Spiniello et al. 2024); galaxies that are believed to have formed only through a single epoch of star formation at early times with no subsequent assembly events. Given its relatively larger size compared to canonical relics, one might expect SNL-1 to have experienced a small amount of minor mergers that contributed to its size growth. It is possible that such events brought in much of the gas that is observed in the present day. While this gas resides in a region where the stellar velocity dispersion is in excess of 300 km s^{-1}, the molecular gas itself is observed to be cold ($\lesssim$10 km s^{-1}; Poci, Smith & Davis, in preparation). However, it has been proposed by low-redshift observations that even cold gas in such extreme physical conditions can be prevented from forming stars due to the shear disrupting the molecular clouds that would otherwise exist (Liu et al. 2021; Davis et al. 2022; Lu et al. 2025). This may be why the SFH exhibits no signs of recent ($t < 13$ Gyr) star formation activity.

SNL-1 also harbours compact nuclear gaseous and old stellar discs, and a prominent nuclear dust disc. The presence and structure of these discs (Section 5), the morphology of the dust on larger spatial scales, as well as the best-fitting 3D orientation from the stellar dynamical model, provide circumstantial evidence for a stellar bar. Our dynamical modelling method does not explicitly account for bars, and the models occupy stationary gravitational potentials. However, using mock data for barred galaxies, Zhu et al. (2018) showed that the recovered physical properties of the model, including the internal orbital properties, are not significantly affected in the presence of a bar. Should a bar be present, it is likely to be at least 10 Gyr old, based on the age of the nuclear stellar disc (de Sá-Freitas et al. 2023). Such old bars have been seen previously in spiral galaxies (Gadotti et al. 2015; Martig et al. 2021). Should an old bar be present in SNL-1, it may imply a relative dearth of violent mergers over the evolutionary history of SNL-1. We note that this does not exclude the occurrence of minor mergers. Martig et al. (2021) found that minor mergers do not destroy the bar, since most of the incoming stars are deposited in the outskirts of the central galaxy (Oser et al. 2010; Karademir et al. 2019).

A key motivation for the MUSE NFM data was resolving the SMBH of SNL-1. Taking our best-fitting value of $M_\bullet = (1.62^{+0.056}_{-0.054}) \times 10^9\,\mathrm{M}_\odot$, the expected sphere of influence is $\sim$73 pc – which is above the spatial resolution of the NFM data. It can also be seen from Fig. 6 that the constraint on $M_\bullet$ is unambiguous. Although large, the measured $M_\bullet$ is completely consistent with the $M_\bullet$–σ relation of Kormendy & Ho (2013). We can therefore exclude a peculiar SMBH mass – both unusually massive and unusually undermassive – as a contributor to the observed discrepancy between the IMF inferences. Moreover, there is no evidence of nuclear activity, such as active galactic nuclei/outflows. Thus, while the central region is structurally complex, there does not appear to be anything occurring in the galaxy nucleus that could influence our interpretation of the spectral measurements.

6.1 IMF tension

The contention around SNL-1 originates from the apparently contradictory results from mass-based and spectroscopic analyses. Measurements of the mass (and mass-to-light ratios) are consistent with a Kroupa (2002) IMF, while spectral analyses simultaneously indicate a relative overabundance of low-mass stars. In this work, we find similar results. Our dynamical analysis provides one measure of the $M_\star/L_{F814W}$, since the mass model is derived from the flux in the $F814W$ band. The dynamical model is consistent with $M_\star/L_{F814W} \sim 2.3$. Conversely, our spectral fits are consistent with $M_\star/L_{F814W} \sim 3.5$. At face value, this implies a dynamical mismatch parameter $\alpha_{\rm IMF} \sim 0.65$. Moreover, the spectral analysis finds that the central region of SNL-1 is consistent with a low-mass IMF slope $\alpha \approx \alpha_{\rm Salpeter}$. This implies an abundance of dwarf stars significantly higher than a MW-like IMF.

A possible resolution (though not the only one) to the above tension proposed previously (Smith 2014) suggests that the two techniques probe different physical scales of the galaxy. In that scenario, the spectral analyses are biased towards the centre of the galaxy, owing to the fact that the (bright) central stellar populations dominate the spectral signatures. Conversely, the lensing/dynamical analyses provide a more global mass estimate, which would contain greater contributions from the outer, supposedly less extreme, stellar populations. We are able to exclude this as a possible resolution to the tension, as our spectral and dynamical analyses are carried out over the same FoV. We have seen that spatial gradients in these properties over this FoV are minimal, and yet the discrepancy persists. This is seen similarly in Lu et al. (2024).

The different measurement techniques are, however, sensitive to different regions of the IMF (e.g. Lu et al. 2023). In the case of ALF, as used in this work, the 'IMF' parameter is probing the mass range $m_\star \in [0.08, 1.0)\,\mathrm{M}_\odot$. Alternatively, for example, the free parameter of the Vazdekis et al. (1996) IMF, and its subsequent incarnations (e.g. Martín-Navarro et al. 2019), constrains the mass range $m_\star \in [0.4, 72)\,\mathrm{M}_\odot$. Smith (2020) describes in detail the variety of assumptions intrinsic to the different spectral-fitting approaches. Yet in contrast to spectral analyses, dynamical/mass-based measurements are naturally sensitive to the full mass range of the IMF, given that they probe the integral over every episode of star formation in a galaxy's history. As such, we might not expect these measurements

[6] ALF measures single stellar population (SSP) equivalent properties, meaning there is no constraint on the SFH of a given spectrum. To explore the SFH, we have additionally fit the same spectra in PPXF using the E-MILES (Vazdekis et al. 2016) SSP library built on the 'BaSTI' isochrones (Pietrinferni et al. 2004) at fixed Kroupa (2002) IMF. As expected, the SFH is extremely short, with no weight given to models with $t < 13$ Gyr. Although the underlying models and fitting methodologies differ, we see consistent constraints on the age of SNL-1 between PPXF and ALF.

to agree even in principle. For example, when compared to measurements from ALF, the mass (and mass-to-light ratio) methods might disagree for any value of $\alpha_{\rm high} \neq \alpha_{\rm Salpeter}$, where $\alpha_{\rm high}$ is the unknown true slope of the IMF over $m_\star \in [1, 100]\,{\rm M}_\odot$. The fitting approach in ALF is justifiably driven by the lack of observational constraints on the high-mass end of the IMF for (even mildly) old integrated stellar spectra, but it means that comparisons to other techniques must be more cautious. Different mass regions of the IMF could be sensitive to, among other things, multiple epochs of star formation (den Brok et al. 2024), which would be captured by mass-based measurements but not spectral analyses. Direct constraints on the high-mass end of the IMF can be obtained using resolved studies of actively star-forming regions (e.g. Yan, Jerabkova & Kroupa 2023), notwithstanding the complication of extremely short lifetimes of the most massive stars (Wirth et al. 2022). But even in this case, such samples would be restricted to the small range of physical conditions found in the solar neighbourhood, and unable to explore the expected dependence of the IMF on, for instance, metallicity (e.g. Martín-Navarro et al. 2015), density (e.g. Poci et al. 2022), and natal conditions (Cameron et al. 2024). More importantly, it is unknown whether those results could be translated to the conditions present in ETGs, in any case.

It is possible, then, that the reported tension in the literature is dramatically weaker or entirely resolved simply by the fact that the different measurement techniques are sensitive to different mass regimes of the IMF. Interestingly, Smith (2020) finds that if the differences in the mass-to-light ratios are to be accounted for solely through the differences in the methodologies, the low-mass cut-off mass of the IMF, $m_{\rm cut}$, would need to be $\sim$0.15 ${\rm M}_\odot$. This is because increasing the $m_{\rm cut}$ would significantly lower the spectroscopic $M_\star/L$, without affecting the spectral fit (since such low-mass stars do not contribute any light to the spectrum anyway).

Unfortunately, empirically constraining $m_{\rm cut}$ is difficult. On one hand, a high abundance of stars below this mass has been detected within the MW (e.g. Sollima 2019), implying that they readily form. Similarly, the spectral fits of Conroy et al. (2017) seem to require a monotonic increase in the number of stars inversely proportional to their mass, all the way down to the hydrogen-burning limit of $m_\star = 0.08\,{\rm M}_\odot$. Chabrier, Hennebelle & Charlot (2014) find that in extreme densities and turbulent gas, the peak mass of the IMF shifts towards lower mass with respect to spiral galaxy (e.g. MW)-like conditions. They find that these conditions are conducive to IMF more dwarf-rich than even that of Salpeter (1955). On the other hand, however, the simulations of Bate (2023) show that at high redshift, there could be significant variation in $m_{\rm cut}$ as a function of metallicity, such that star formation at solar metallicity at $z = 5$ produces a mass function which is deficient in stars with $m_\star \lesssim 0.10\,{\rm M}_\odot$. Having solar metallicity by $z = 5$ implies a chemical enrichment history which was very rapid, but one which is compatible with the data of SNL-1. Elevated $m_{\rm cut}$ has also been inferred from observations in Barnabè et al. (2013), by anchoring the expectation from the spectral fitting to that from lensing and stellar dynamics. There, circumstantial evidence for $m_{\rm cut} \approx 0.1$–$0.15\,{\rm M}_\odot$ was found for two massive ETGs using high-resolution aperture spectra. Newman et al. (2017) also tested for the variation of $m_{\rm cut}$ by including it as a free parameter in their spectral fits, and found a peak in the posterior at $m_{\rm cut} = 0.15\,{\rm M}_\odot$ for SNL-1. We redid the spatially integrated spectral fit discussed in Appendix D, but this time allowing $m_{\rm cut}$ to vary. This fit has a best-fitting $m_{\rm cut} \approx 0.35^{+0.0064}_{-0.19}\,{\rm M}_\odot$. Despite the high S/N of this integrated spectrum, the posterior distribution of $m_{\rm cut}$ is still broad. We conclude that $m_{\rm cut}$ is unconstrained by the data, especially for the spatially resolved spectra. Consequently, resolving the apparent tension in the literature will require higher quality data and improved models. Nevertheless, if the scenario described in Smith (2020) is applicable to SNL-1 and its IMF had a relatively high $m_{\rm cut}$, differences in the modelled mass ranges of the IMF may partially resolve the observed discrepancy in the $M_\star/L$. Whether this can fully explain the observations, however, remains to be seen.

7 CONCLUSION

We have analysed new VLT/MUSE NFM data of a nearby strong lens, SNL-1. We have applied flexible spectral and dynamical methods to disentangle the contributions to the mass budget in the nuclear region. In particular, we have measured the IMF with high spatial resolution and sought to resolve an existing tension between different measurement techniques. Our results are summarized here:

(i) Dynamically, we modelled a previously undetected nuclear stellar disc. We find it to be highly flattened, embedded in a largely elliptical mass distribution. The new data allow us to directly constrain the mass of the central SMBH. We measure $M_\bullet = (1.62^{+0.056}_{-0.054}) \times 10^9\,{\rm M}_\odot$.

(ii) Spectroscopically, we have measured a variety of stellar population properties. SNL-1 is extremely old, and relatively metal-rich. It is enhanced in many of the individual chemical abundances, especially [Na/H] and [O/H], but with very little spatial variation over the small central region probed here. Under the assumptions of ALF regarding the shape of the IMF and its mass limits, we have measured relatively dwarf-rich populations across the entire nuclear region, with a IMF slope of $\alpha \approx \alpha_{\rm Salpeter}$, for the mass range $m_\star \in [0.08, 1.0)\,{\rm M}_\odot$.

(iii) At face value, we have recovered the existing tension in the literature regarding the IMF as measured by different methodologies. Peculiarly, the spectra predict overmassive populations with respect to the dynamics. Several causes suggested previously are excluded, including differences in the physical scales probed by each method, as well as unresolved non-stellar contributions (e.g. an unaccounted for SMBH). With the flexibility of the models applied here, we can also rule out the presence of some biases in earlier works, such as assumptions on the orbital isotropy. Yet we conclude that a 'tension' itself may not be physically present, and rather caution the comparison of disparate measurement techniques, especially when it concerns the IMF.

In general, future observations at this spatial scale will prove critical to understanding past IMF studies, and indeed the central regions of ETGs more broadly. In a forthcoming work, we will jointly model multiscale, multitracer data for SNL-1, in order to confirm the nuclear structure inferred in this work, and its implications for the IMF. Ultimately, the conundrum of the IMF in SNL-1 remains. This tension cannot be decoupled from its intrinsic physical properties and complicated nuclear structures, which are also yet to be fully characterized. Multiscale, multitracer data may help in breaking any degeneracies, in particular of the existing mass-based models. However, the evidence indicates that something intrinsic, at least for SNL-1, is favouring these contradictory results. The complex structures present in the core of SNL-1 indicate that it may not be the ideal candidate for benchmark studies of various IMF techniques. Thus, the task remains to understand the intricate spectral signatures and dynamical structures in order to robustly measure the IMF in external galaxies.

ACKNOWLEDGEMENTS

We thank Tim Davis, Dimitri Gadotti, and Chiara Spiniello for many insightful discussions. AP acknowledges support from the Hintze Family Charitable Foundation. AP and RJS acknowledge support from the Science and Technology Facilities Council through the Durham Astronomy Consolidated Grants 2023–2026 (ST/T000244/1andST/X001075/1). This research is based on observations collected at the European Organisation for Astronomical Research in the Southern Hemisphere under ESO programme 109.22X3.001. This work used the DiRAC at Durham facility managed by the Institute for Computational Cosmology on behalf of the STFC DiRAC HPC Facility (www.dirac.ac.uk). The equipment was funded by BEIS capital funding via STFC capital grants ST/K00042X/1,ST/P002293/1,ST/R002371/1, and ST/S002502/1, Durham University, and STFC operations grant ST/R000832/1. DiRAC is part of the National e-Infrastructure. This work utilized existing software packages for data analysis and presentation, including ASTROPY (Astropy Collaboration 2013), CYTHON (Behnel et al. 2011), IPYTHON (Perez & Granger 2007), MATPLOTLIB (Hunter 2007), NUMPY (Harris et al. 2020), the SCIPY ecosystem (Virtanen et al. 2020), STATSMODELS (Seabold & Perktold 2010), and SEABORN (Waskom 2021). We thank the anonymous referees for their constructive comments that improved the quality and clarity of this work.

DATA AVAILABILITY

The observational data used in this work are publicly available in the ESO archive (archive.eso.org). Other products can be provided upon reasonable request to the author.

REFERENCES

Alton P. D., Smith R. J., Lucey J. R., 2018, MNRAS, 478, 4464
Arsenault R. et al., 2008, in Hubin N., Max C. E., Wizinowich P. L., eds, Proc. SPIE Conf. Vol. 7015, Adaptive Optics Systems. SPIE, Bellingham, p. 701524
Astropy Collaboration, 2013, A&A, 558, A33
Athanassoula E., Bureau M., 1999, ApJ, 522, 699
Bacon R. et al., 2010, in McLean I. S., Ramsay S. K., Takami H., eds, Proc. SPIE Conf. Vol. 7735, Ground-Based and Airborne Instrumentation for Astronomy III. SPIE, Bellingham, p. 773508
Barnabè M., Spiniello C., Koopmans L. V. E., Trager S. C., Czoske O., Treu T., 2013, MNRAS, 436, 253
Bate M. R., 2023, MNRAS, 519, 688
Behnel S., Bradshaw R., Citro C., Dalcin L., Seljebotn D. S., Smith K., 2011, Comput. Sci. Eng., 13, 31
Brewer B. J. et al., 2012, MNRAS, 422, 3574
Cameron A. J., Katz H., Witten C., Saxena A., Laporte N., Bunker A. J., 2024, MNRAS,534,523
Cappellari M., 2002, MNRAS, 333, 400
Cappellari M., 2016, ARA&A, 54, 597
Cappellari M., 2017, MNRAS, 466, 798
Cappellari M., Copin Y., 2003, MNRAS, 342, 345
Cappellari M., Emsellem E., 2004, PASP, 116, 138
Chabrier G., Hennebelle P., Charlot S., 2014, ApJ, 796, 75
Cheng C. M., Villaume A., Balogh M. L., Brodie J. P., Martín-Navarro I., Romanowsky A. J., van Dokkum P. G., 2023, MNRAS, 526,4004
Collier W. P., Smith R. J., Lucey J. R., 2018a, MNRAS, 473, 1103
Collier W. P., Smith R. J., Lucey J. R., 2018b, MNRAS, 478, 1595
Conroy C., van Dokkum P. G., Villaume A., 2017, ApJ, 837, 166
Conroy C., Villaume A., van Dokkum P. G., Lind K., 2018, ApJ, 854, 139
Davis T. A., McDermid R. M., 2017, MNRAS, 464, 453
Davis T. A. et al., 2022, MNRAS, 512, 1522
Deeley S., Drinkwater M. J., Sweet S. M., Bekki K., Couch W. J., Forbes D. A., 2023, MNRAS, 525, 1192
Della Bruna L. et al., 2022, A&A, 660, A77
den Brok M., Krajnović D., Emsellem E., Mercier W., Steinmetz M., Weilbacher P. M., 2024, MNRAS, 530, 3278
de Sá-Freitas C. et al., 2023, A&A, 671, A8
de Zeeuw T., Franx M., 1991, ARA&A, 29, 239
Dutton A. A., Macciò A. V., 2014, MNRAS, 441, 3359
Dutton A. A., Mendel J. T., Simard L., 2012, MNRAS, 422, L33
Emsellem E. et al., 2022, A&A, 659, A191
Fétick R. J. L. et al., 2019, A&A, 628, A99
Foreman-Mackey D., Hogg D. W., Lang D., Goodman J., 2013, PASP, 125, 306
Gadotti D. A., Seidel M. K., Sánchez-Blázquez P., Falcón-Barroso J., Husemann B., Coelho P., Pérez I., 2015, A&A, 584, A90
Grèbol-Tomàs P., Ferré-Mateu A., Domínguez-Sánchez H., 2023, MNRAS,526,4024
Gu M., Greene J. E., Newman A. B., Kreisch C., Quenneville M. E., Ma C.-P., Blakeslee J. P., 2022, ApJ, 932, 103
Harris C. R. et al., 2020, Nature, 585, 357
Hunter J. D., 2007, Comput. Sci. Eng., 9, 90
Kam Z. S., Carignan C., Chemin L., Amram P., Epinat B., 2015, MNRAS, 449, 4048
Karademir G. S., Remus R.-S., Burkert A., Dolag K., Hoffmann T. L., Moster B. P., Steinwandel U. P., Zhang J., 2019, MNRAS, 487, 318
Kormendy J., Ho L. C., 2013, ARA&A, 51, 511
Krajnović D. et al., 2008, MNRAS, 390, 93
Kroupa P., 2001, MNRAS, 322, 231
Kroupa P., 2002, Science, 295, 82
La Barbera F., Vazdekis A., Ferreras I., Pasquali A., Allende Prieto C., Röck B., Aguado D. S., Peletier R. F., 2017, MNRAS, 464, 3597
La Barbera F. et al., 2019, MNRAS, 489, 4090
La Barbera F., Vazdekis A., Ferreras I., Pasquali A., 2021, MNRAS, 505, 415
Liu L., Bureau M., Blitz L., Davis T. A., Onishi K., Smith M., North E., Iguchi S., 2021, MNRAS, 505, 4048
Lu S., Zhu K., Cappellari M., Li R., Mao S., Xu D., 2023, MNRAS, 526, 1022
Lu S., Zhu K., Cappellari M., Li R., Mao S., Xu D., 2024, MNRAS, 530, 4474
Lu A. et al., 2025, MNRAS, 531, 3888
Lyubenova M. et al., 2016, MNRAS, 463, 3220
Martig M. et al., 2021, MNRAS, 508, 2458
Martín-Navarro I. et al., 2015, ApJ, 806, L31
Martín-Navarro I. et al., 2019, A&A, 626, A124
Martín-Navarro I. et al., 2021, A&A, 654, A59
Massey R., Stoughton C., Leauthaud A., Rhodes J., Koekemoer A., Ellis R., Shaghoulian E., 2010, MNRAS, 401, 371
Mitchell C. J., Williams T. B., Spekkens K., Lee-Waddell K., Kuzio de Naray R., Sellwood J. A., 2015, AJ, 149, 116
Naab T., Johansson P. H., Ostriker J. P., 2009, ApJ, 699, L178
Navarro J. F., Frenk C. S., White S. D. M., 1996, ApJ, 462, 563
Newman A. B., Smith R. J., Conroy C., Villaume A., van Dokkum P., 2017, ApJ, 845, 157
Oser L., Ostriker J. P., Naab T., Johansson P. H., Burkert A., 2010, ApJ, 725, 2312
Parikh T., Saglia R., Thomas J., Mehrgan K., Bender R., Maraston C., 2024, MNRAS, 528,7338
Perez F., Granger B. E., 2007, Comput. Sci. Eng., 9, 21
Pietrinferni A., Cassisi S., Salaris M., Castelli F., 2004, ApJ, 612, 168
Planck Collaboration VI, 2020, A&A, 641, A6
Poci A., Smith R. J., 2022, MNRAS, 512, 5298
Poci A., McDermid R. M., Zhu L., van de Ven G., 2019, MNRAS, 487, 3776
Poci A. et al., 2022, MNRAS, 514, 3660
Salpeter E. E., 1955, ApJ, 121, 161
Schwarzschild M., 1979, ApJ, 232, 236
Seabold S., Perktold J., 2010, in van der Walt S., Millman J., eds, Proceedings of the 9th Python in Science Conference (SciPy 2010). SciPy, Austin, TX, p. 92

Smith R. J., 2014, MNRAS, 443, L69
Smith R. J., 2020, ARA&A, 58, 577
Smith R. J., Lucey J. R., Conroy C., 2015a, MNRAS, 449, 3441
Smith R. J., Alton P., Lucey J. R., Conroy C., Carter D., 2015b, MNRAS, 454, L71
Sollima A., 2019, MNRAS, 489, 2377
Spekkens K., Sellwood J. A., 2007, ApJ, 664, 204
Spiniello C., Koopmans L. V. E., Trager S. C., Czoske O., Treu T., 2011, MNRAS, 417, 3000
Spiniello C. et al., 2024, MNRAS,527, 8793
Ströbele S. et al., 2012, in Ellerbroek B. L., Marchetti E., Véran J.-P., eds, Proc. SPIE Conf. Vol. 8447, Adaptive Optics Systems III. SPIE, Bellingham, p. 844737
van den Bosch R. C. E., van de Ven G., Verolme E. K., Cappellari M., De Zeeuw P. T., 2008, MNRAS, 385, 647
van der Marel R. P., Franx M., 1993, ApJ, 407, 525
van Dokkum P., Conroy C., Villaume A., Brodie J., Romanowsky A. J., 2017, ApJ, 841, 68
Vaughan S. P., Davies R. L., Zieleniewski S., Houghton R. C. W., 2018, MNRAS, 475, 1073
Vazdekis A., Casuso E., Peletier R. F., Beckman J. E., 1996, ApJS, 106, 307
Vazdekis A., Koleva M., Ricciardelli E., Röck B., Falcón-Barroso J., 2016, MNRAS, 463, 3409
Verro K. et al., 2022, A&A, 660, A34
Villaume A., Conroy C., Johnson B., Rayner J., Mann A. W., van Dokkum P., 2017, ApJS, 230, 23
Virtanen P. et al., 2020, Nat. Methods, 17, 261
Waskom M. L., 2021, J. Open Source Softw., 6, 3021
Weilbacher P. M. et al., 2020, A&A, 641, A28
Wirth H., Kroupa P., Haas J., Jerabkova T., Yan Z., Šubr L., 2022, MNRAS, 516, 3342
Yan Z., Jerabkova T., Kroupa P., 2023, A&A, 670, A151
Zhu L. et al., 2018, MNRAS, 473, 3000
Zibetti S., Gallazzi A. R., Hirschmann M., Consolandi G., Falcón-Barroso J., van de Ven G., Lyubenova M., 2020, MNRAS, 491, 3562

APPENDIX A: SKY CTI ISSUES

The science spectra from the pipeline-reduced data cube exhibited strange sky emission-line shapes, characterized by a strong oversubtraction and strong undersubtraction on neighbouring spectral pixels around the emission-line wavelength. To investigate the cause of this issue, we set about analysing the input data at each stage of the reduction pipeline. From this, it became apparent that the dedicated offset sky frames were problematic, which we believe is caused by charge transfer inefficiency (CTI) effects. We describe our process and conclusions in this section.

The MUSE data reduction pipeline (Weilbacher et al. 2020) includes a sophisticated sky modelling treatment, which distinguishes between line and continuum components. For observations of targets that fill the MUSE FoV, as in our case, this sky model is derived from a blank sky field observed close in time to the science exposure. The model includes a description of the LSF and its variation with position and wavelength. This LSF is used, in combination with the modelled fluxes of known emission lines, to build the line component of the sky, which varies on rapid time-scales. The fluxes of different groups of emission lines vary in lockstep, so that the amplitudes of the groups can be adjusted when transferring the line model to the science data. The continuum component is assumed to vary only on longer time-scales, and is subtracted from the science data without modification.

In general, the blank sky exposure is much shorter than the science observations, since it is assumed that the sky information is pooled from all $\sim 10^5$ spatial pixels. For each of the six OBs of our observation, the sky exposures were 120 s, compared to 2257–2574 s for the science target (depending on the overheads). With the 25 mas pixel size of NFM observations in particular, the short-exposure sky frames lead to extremely low count levels. Indeed, in our 120 s exposures, the (clipped) mean pixel value is 0.27 e^- above the bias level, i.e. most pixels receive no photons during the exposure. Under such conditions, CCD images exhibit artefacts caused by charge being temporarily retained by empty 'traps' in the silicon lattice during readout. One observable consequence of such CTI effects is the formation of near-exponential trails behind sources, extended away from the readout direction, caused by the late arrival of temporarily trapped charge (e.g. see Massey et al. 2010). By contrast, in much longer exposures (e.g. the science frames), or for MUSE WFM observations with 64 times larger pixel area, most charge traps will be filled during the exposure, and become unable to retain electrons during the readout phase.

In the case of our MUSE NFM blank sky observations, trails likely due to CTI effects are clearly observable in the observed sky line profiles, as seen in the mean calibrated spectrum (see Fig. A1). Sky lines in the red part of the spectrum fall in the upper quadrants of the CCD, and are readout to amplifiers at the top; these lines show an asymmetric wing towards the blue. By contrast, the 5577 Å line falls in the lower quadrants, which are readout to amplifiers at the bottom, and the line profile asymmetry is reversed as expected.

The asymmetric line profiles are observed only in the short blank-sky observations, and not in the sky lines in the science data. Since the pipeline assumes the LSF is identical between the sky and target observations, the 'line' component cannot respond to the presence of the wings. Instead, they are absorbed into the sky 'continuum' component, which then includes highly asymmetric features slightly offset from each sky line, which we believe causes the sharp oversubtraction/undersubtraction.

We tested many avenues to account for the CTI issues in the sky frames before including them in the data reduction process. For example, we attempted to include a correction to the sky lines, which depended on the readout direction of each line. We also tried to smooth the continuum component of the sky model, which should be where the asymmetry from the sky emission lines is absorbed, before folding it back into the data reduction. All of these attempts resulted in significant systematic noise being introduced to the science frames because of the low signal present in the sky frames to begin with.

In the end, we constructed a spectrum from a small annulus at the exterior of the raw science cube ($\sim$3.5 arcsec/2.26 kpc radius from the galaxy centre), which contains sky and some signal from the science target. We then subtracted that spectrum from the full raw science cube to obtain our ad hoc 'sky-subtracted' cube. The motivation for this is that the sky should have a constant shape and surface brightness across the FoV, while the steep decline in surface brightness of the target means that its signal is relatively unaffected within our science aperture of 0.6 arcsec radius.

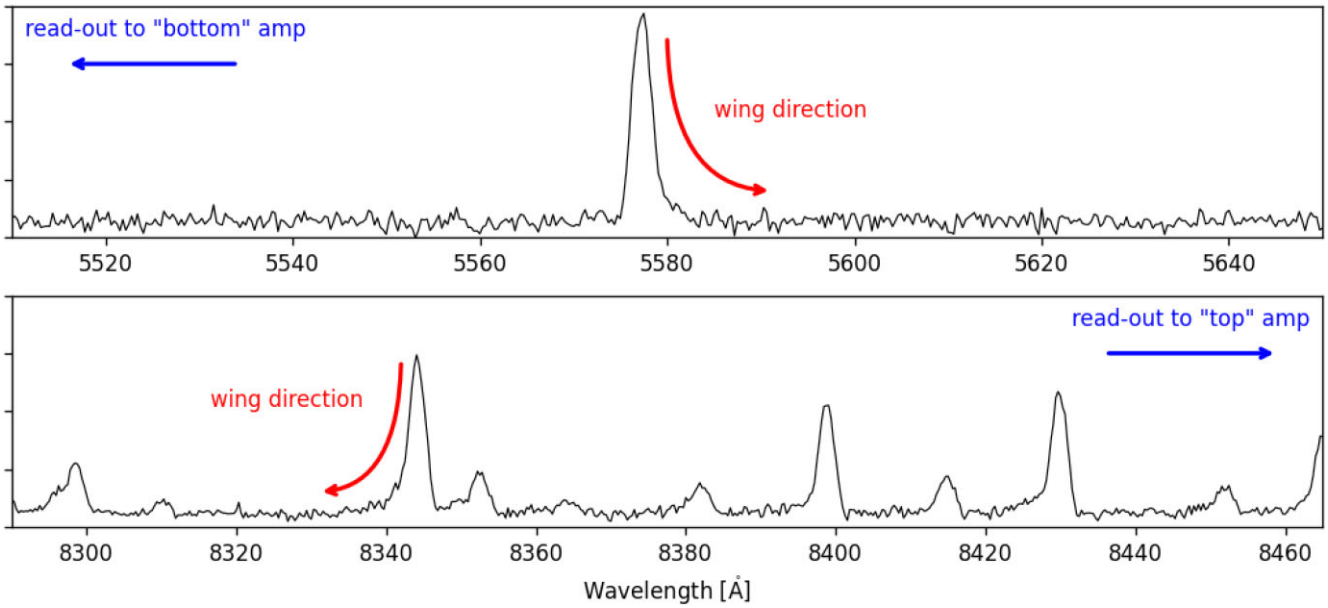

Figure A1. Profiles of sky emission lines, binned over large areas of the short offset-sky cubes, showing CTI-induced wings extending away from the amplifier.

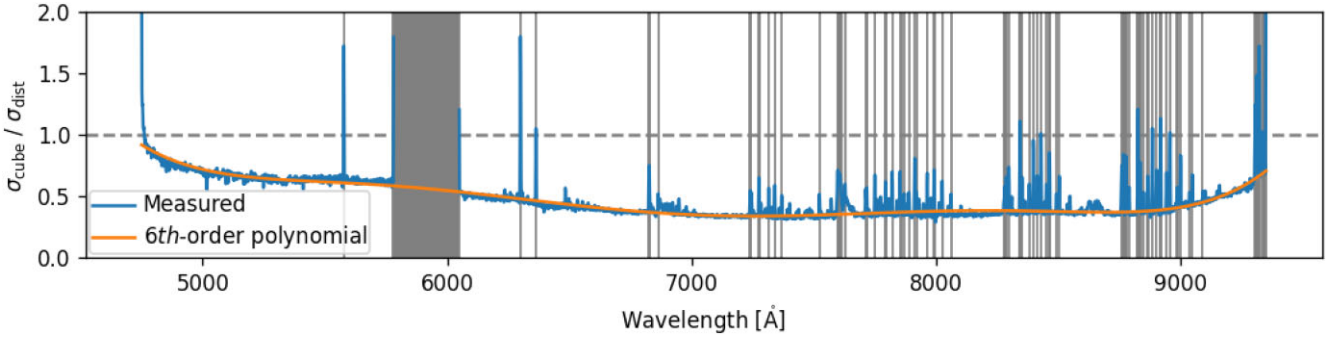

Figure B1. Ratio spectrum of the mean reported uncertainty across a small spatial patch σ_{cube} to the estimated true observational uncertainty over that same region σ_{dist}, shown in blue. A sixth-order polynomial fit to the continuum of the ratio spectrum is shown in orange. The emission-line masking is shown in grey. The polynomial fit is used to scale the data cube uncertainties.

APPENDIX B: DATA CUBE ERRORS

During the data analysis, we noted that the error cube provided by the standard ESO pipeline appeared to be significantly underestimated, based on the noisy appearance of spectra with an apparently high formal S/N. This has also been seen in other data sets (see Emsellem et al. 2022, for a discussion). We endeavoured to quantify and rectify this for our data cube. To this end, we first isolated a number of small (20×20 pixels) spatial patches in the outskirts of SNL-1 (outside the eventual science aperture), within which we assume that the intrinsic galactic variations are negligible. We computed the distribution of fluxes using every spaxel within a given spatial patch, for every wavelength channel. Taking the standard deviation of each distribution, σ_{dist}, results in a spectrum of the true observational uncertainty. We repeated this for every spatial patch to check for large-scale variations, finding that the error spectra were consistent across the different spatial patches. Comparing σ_{dist} to the mean reported uncertainty from the data cube over the same spatial region, σ_{cube}, provides an estimate for how much the latter is underestimated. We fit a general sixth-order polynomial to the spectrum of the ratio $\sigma_{cube}/\sigma_{dist}$ (masking the sky lines). We then scale the data cube uncertainties by this polynomial to arrive at an uncertainty-corrected data cube, which we use throughout this work. The uncertainty spectrum and polynomial fit are shown in Fig. B1. We find that the ratio is typically $\sim$0.5 across the spectral range, implying that the formal uncertainties are underestimated by a factor of 2. This is larger than what was found in Emsellem et al. (2022), who used a different approach to estimate this level and found a $\sim$10–30 per cent underestimation.

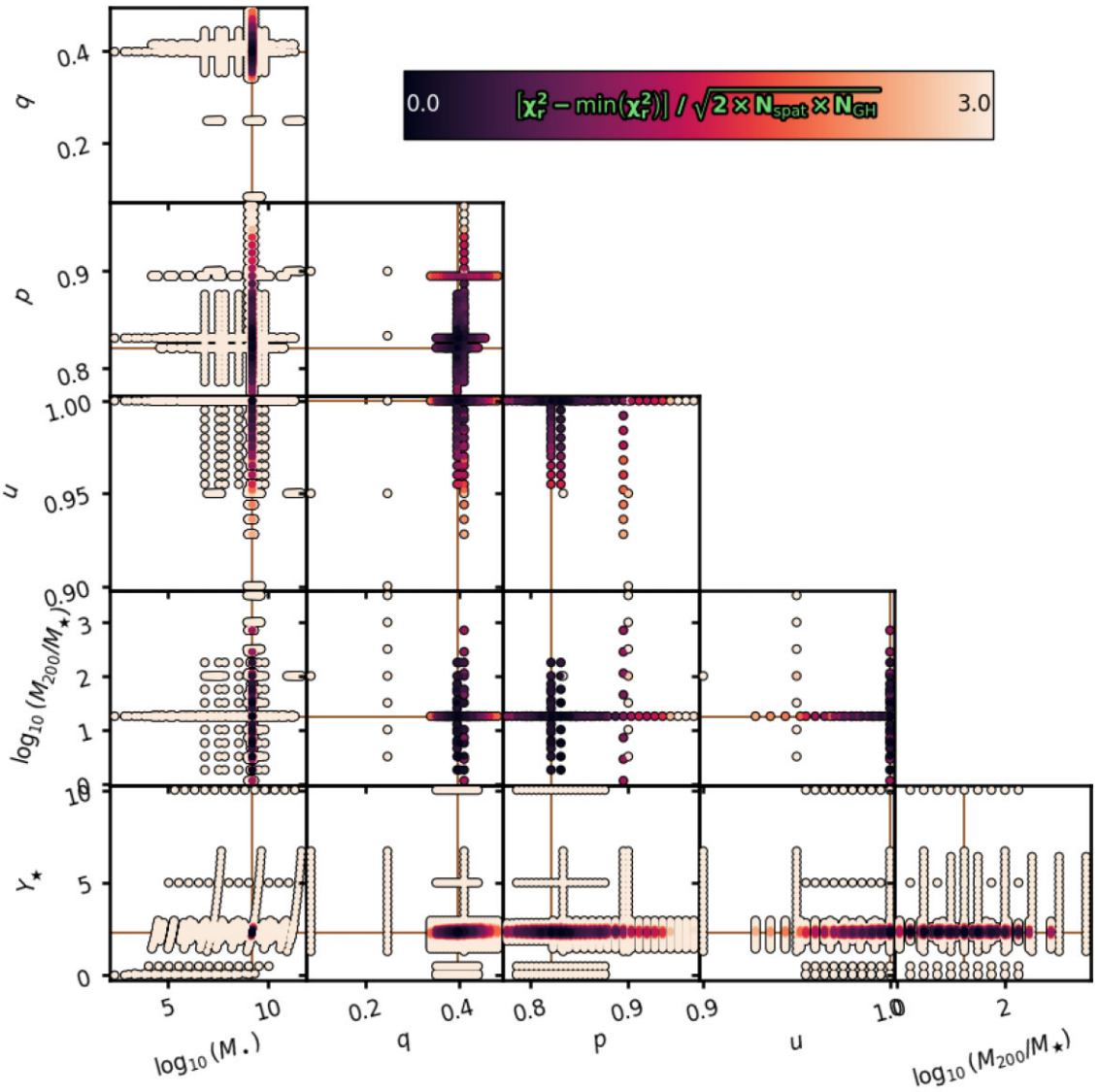

Figure C1. As Fig. 6, but showing the full range of parameters explored.

APPENDIX C: SCHWARZSCHILD MODEL PARAMETER-SPACE EXPLORATION

In Fig. C1, we show the full extent of the physical parameters explored for the Schwarzschild model in searching for the best fit.

APPENDIX D: FULL ALF FIT TO APERTURE SPECTRUM

ALF employs a multidimensional fitting routine in order to be able to measure an array of chemical abundances and other stellar properties. As a consequence, a fit including all the flexibility in ALF requires input spectra with very high S/N; 100 or greater (e.g. Cheng et al. 2023). As a combination of the CTI issues discussed above, coupled with the small pixel size of the NFM, our data do not meet this S/N even with significant spatial binning. By instead limiting the flexibility of the ALF fit, we prevent broad variations of some elemental abundances which in practice would be largely unconstrained. Unconstrained variations in those abundances could trade off with other parameters of the fit which we are directly interested in, especially in the presence of noise. Thus, removing the ability of those abundances to vary in principle produces more stable solutions for the parameters we are interested in.

We first constructed a single spectrum by integrating over the entire FoV (that which is shown in Fig. 5), resulting in a spectrum with S/N = 550. This is then fit with the full flexibility of ALF, including all individual elemental abundances, jitter and instrumental terms, and kinematic moments V, σ, $h3$, and $h4$. We keep the same parametrization of the IMF, being a two-part power law over the mass range $m_\star \in [0.08, 100]\,\mathrm{M}_\odot$, with free lower mass slope α_1 over $m_\star \in [0.08, 1.0)\,\mathrm{M}_\odot$, and fixed $\alpha_{\mathrm{Salpeter}} = 2.3$ for $m_\star \geq 1.0\,\mathrm{M}_\odot$. This fit is shown in Fig. D1. We show a subset of the posteriors in Fig. D2 for clarity, to assess the correlations between the elemental abundances.

We adopt the values of [Si/H], [K/H], [V/H], [Cr/H], [Mn/H], [Co/H], [Ni/H], [Cu/H], [Sr/H], [Ba/H], and [Eu/H] from this fit for all subsequent fits to the individual spectra binned to S/N = 80. The stellar properties of the integrated fit, including the values to which the listed elemental abundances are fixed, are given in Table D1.

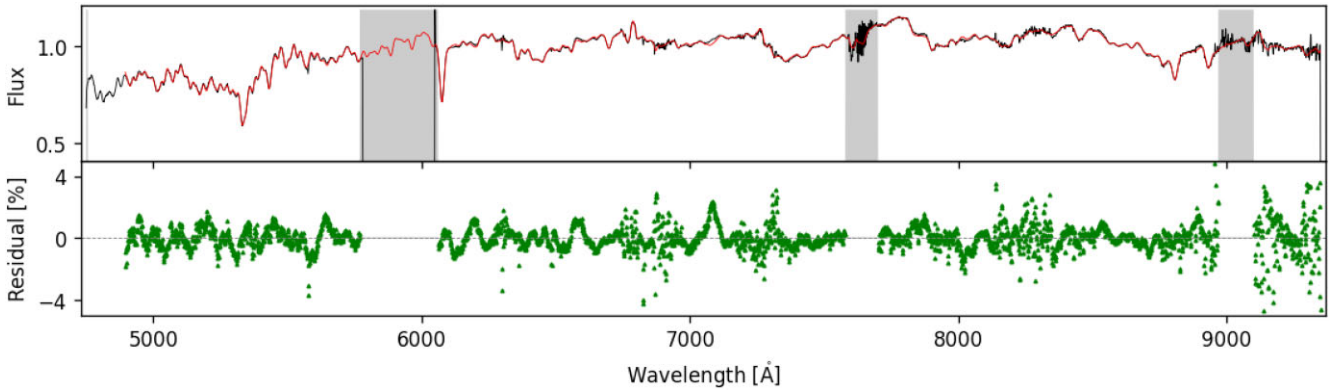

Figure D1. Top: Spatially integrated spectrum of SNL-1 (black) and the ALF fit (red). Bottom: Normalized residuals of the fit [100 × (data − model)/data].

The implicit assumption in this approach is that there are no (strong) spatial gradients of those particular elemental abundances, but in practice we only care that they do not introduce a systematic bias in any of the parameters we are actually interested in, such as the IMF slope.

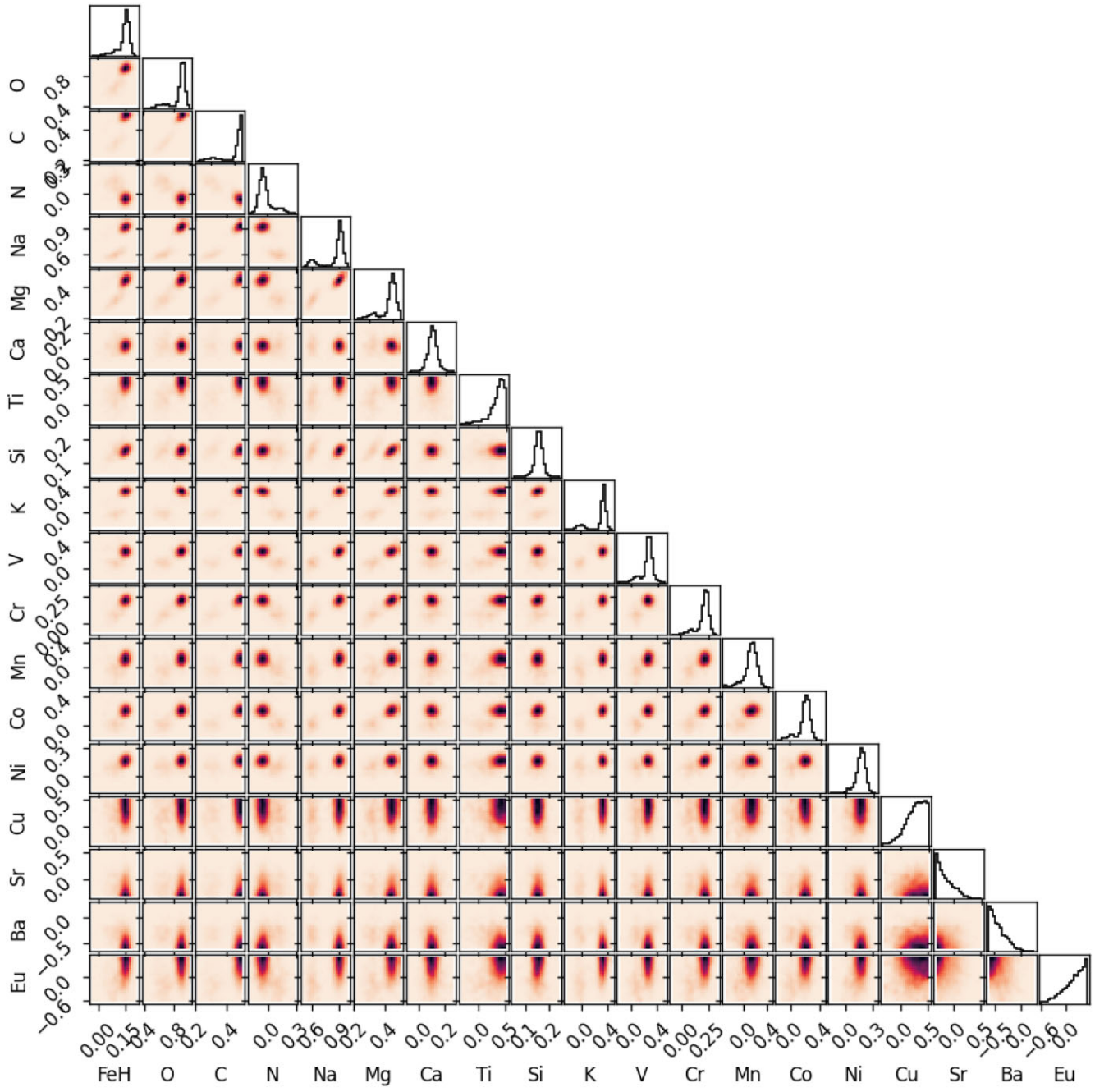

Figure D2. Posterior distributions from the fully flexible fit to the 1.25 arcsec integrated aperture spectrum. All elemental abundances in ALF are shown. The cross-panels are density maps of the underlying MCMC chain for clarity, with dark regions corresponding to higher likelihoods. This figure illustrates that there are no correlations between the abundances we are interested in scientifically and those we keep fixed in subsequent fits.

Table D1. Best-fitting stellar parameters from the 1.25 arcsec integrated aperture spectrum and the associated 1σ uncertainty derived from the posterior distributions. The elemental abundances in the lower part of the table (below titanium [Ti/H]) are held fixed in subsequent spectral fits to the values listed here.

Parameter	Value	1σ
Age $\log_{10}(t$ [Gyr])	1.02	0.03
Metallicity [Z/H]	0.06	0.03
IMF slope α_1	2.28	0.19
Iron [Fe/H]	0.16	0.03
Oxygen [O/H]	0.95	0.10
Carbon [C/H]	0.49	0.07
Nitrogen [N/H]	0.00	0.07
Sodium [Na/H]	0.93	0.12
Magnesium [Mg/H]	0.47	0.05
Calcium [Ca/H]	0.16	0.02
Titanium [Ti/H]	0.35	0.13
Silicon [Si/H]	0.10	0.04
Potassium [K/H]	0.35	0.14
Vanadium [V/H]	0.36	0.08
Chromium [Cr/H]	0.21	0.06
Manganese [Mn/H]	0.11	0.11
Cobalt [Co/H]	0.25	0.09
Nickel [Ni/H]	0.18	0.05
Copper [Cu/H]	0.48	0.17
Strontium [Sr/H]	−0.28	0.14
Barium [Ba/H]	−0.57	0.14
Europium [Eu/H]	0.37	0.25

This paper has been typeset from a TEX/LATEX file prepared by the author.